

**A NEW INTERPRETATION OF CONTROLLED-SOURCE HELICOPTER
ELECTROMAGNETIC SURVEY DATA
SECO CREEK, EDWARDS AQUIFER, TX**

A Thesis

by

KATHRYN TERESA DECKER

Submitted to the Office of Graduate Studies of
Texas A&M University
in partial fulfillment of the requirements for the degree of

MASTER OF SCIENCE

December 2009

Major Subject: Geophysics

**A NEW INTERPRETATION OF CONTROLLED-SOURCE HELICOPTER
ELECTROMAGNETIC SURVEY DATA
SECO CREEK, EDWARDS AQUIFER, TX**

A Thesis

by

KATHRYN TERESA DECKER

Submitted to the Office of Graduate Studies of
Texas A&M University
in partial fulfillment of the requirements for the degree of

MASTER OF SCIENCE

Approved by:

Chair of Committee,
Committee Members,

Head of Department,

Mark E. Everett
Richard Carlson
Cristine Morgan
Andreas Kronenberg

December 2009

Major Subject: Geophysics

ABSTRACT

A New Interpretation of Controlled-Source Helicopter Electromagnetic Survey Data

Seco Creek, Edwards Aquifer, TX. (December 2009)

Kathryn Teresa Decker, B.S. Binghamton University;

B.A. Binghamton University

Chair of Advisory Committee: Dr. Mark Everett

The Edwards aquifer lies in the structurally complex Balcones fault zone and supplies water to the growing city of San Antonio. To ensure that future demands for water are met, the hydrological and geophysical properties of the aquifer must be well-understood. Fractures often occur in a power-law distribution. Fracture distribution plays an important role in determining electrical and hydraulic current flowpaths. The thesis research presents an evaluation of the controlled-source electromagnetic (CSEM) response for layered models with a fractured layer at depth described by the roughness parameter, β_v , such that $0 \leq \beta_v$, associated with the power-law length-scale dependence of electrical conductivity. A value of $\beta_v=0$ represents homogeneous, continuous media, while a value of $0 < \beta_v$ shows that roughness exists. 1-D synthetic modeling shows that the existence of a fractured layer at depth is apparent in the CSEM time-domain response for models representing aquifers. The research also provides an analysis of the Seco Creek frequency-domain helicopter electromagnetic survey data set by introducing the similarly defined roughness parameter β_h to detect lateral roughness along survey

lines. Fourier transforming the apparent resistivity as a function of position along flight line into wavenumber domain using a 256-point sliding window gives the power spectral density (PSD) plot for each line. The value of β_H is the slope of the least squares regression for the PSD in each 256-point window. Changes in β_H with distance along the flight line are plotted. Large values of β_H are found near well-known large fractures and maps of β_H produced by interpolating values of β_H along survey lines suggest unmapped structure at depth.

To my family

ACKNOWLEDGEMENTS

I would like to thank my committee members, and especially my committee chair, for their hours of hard work and helpful editing comments, as well as their thought-provoking questions during my defense.

TABLE OF CONTENTS

		Page
	ABSTRACT.....	iii
	DEDICATION.....	v
	ACKNOWLEDGEMENTS.....	vi
	TABLE OF CONTENTS.....	vii
	LIST OF FIGURES.....	ix
	LIST OF TABLES.....	xi
I	INTRODUCTION.....	1
	1.1 Motivation.....	1
	1.2 Objectives.....	5
II	GEOLOGY AND HYDROLOGY OF THE EDWARDS AQUIFER.....	7
	2.1 The Edwards Aquifer and Surrounding Geology.....	7
	2.2 Depositional Environment of the Edwards Group and Associated Sedimentary Rock Units.....	8
	2.3 Balcones Fault Zone.....	11
	2.4 Stratigraphy and Porosity.....	13
	2.5 Power-law Scaling of Fractures.....	18
III	CLASSICAL INTERPRETATION OF CSEM DATA.....	20
	3.1 Theory.....	20
	3.2 Limitations of Classical Theory.....	25
IV	INHOMOGENEOUS “ROUGH” PLANE LAYERED CASE AND MODELS.....	26

	4.1 Extending Homogeneous Plane Layered Theory to the Inhomogeneous Plane Layered Case.....	26
	4.2 Modeling.....	28
V	HEM SURVEY.....	36
	5.1 Literature Review of Airborne Electromagnetic Surveys.....	36
	5.2 Helicopter EM Survey Details.....	39
VI	DATA ANALYSIS.....	44
	6.1 Resistivity Maps.....	44
	6.2 β_H Maps.....	51
VII	CONCLUSIONS AND RECOMMENDATIONS FOR FURTHER WORK.....	59
	7.1 Conclusions.....	59
	7.2 Recommendations for Further Work.....	61
	REFERENCES.....	62
	APPENDIX.....	66
	VITA.....	75

LIST OF FIGURES

FIGURE	Page
2.1 Representation of depositional geography during the Lower Cretaceous with location of cities indicated for reference.....	9
2.2 Map of Edwards aquifer area with counties labeled.....	12
3.1 Schematic of eddy current diffusion in the subsurface In a ground-based loop configuration.....	22
3.2 Schematic of plane-layered homogeneous earth with heights h_{TX} and h_{RX} labeled to represent the elevation of the HEM equipment.....	24
4.1 Generalized electrical conductivity with power law dependence on length scale L	26
4.2 TEM47 response curves for a 3-layer model with conductivity $\sigma=0.1$ S/m appropriate for shale or wet sandstone.....	30
4.3 TEM47 response for sensitivity to depth, tested by adjusting the depth of the fractured layer.....	31
4.4 TEM47 responses for a dry, resistive sandstone sandwiched between two layers of more conductive shale.....	33
4.5 TEM47 responses for aquifer-based model with fractured middle layer.....	34

FIGURE	Page
5.1 Schematic of the RESOLVE 6 System and photo of system in flight.....	39
5.2 Map of the survey area as an overlay on geological map.....	42
5.3 Geology map over Google Earth Satellite image of field site with survey lines analyzed marked in white.....	43
6.1 Maps of apparent resistivity for the horizontal coplanar coil pairs.....	46
6.2 Plot of the PSD for Line 4.....	48
6.3 Plot of β_H v. position along Line 4.....	50
6.4 Maps of β_H for 18 processed survey lines from the plots of β_H v. position along line.....	51
6.5 The β_H map for 100 kHz is aligned with the survey lines.....	55
6.6 Overlay of β_H map for 400 Hz.....	57
6.7 Overlay of β_H maps for all six frequencies.....	58

LIST OF TABLES

TABLE	Page
2.1 Description of the depositional cycle and associated material properties for the Edwards aquifer rocks.....	10
2.2 Description of the units within the Devils River Formation.....	14
2.3 Description of the units confining the Edwards aquifer.....	14
4.1 Conductivities of common sedimentary aquifer rocks.....	29
5.1 Frequencies and coil orientation for the RESOLVE 6 System.....	40
5.2 Skin depth calculated for a conductivity of 0.01 S/m.....	41

I. INTRODUCTION

1.1 Motivation

The Edwards aquifer supplies all of the residential, agricultural, and industrial water for the city of San Antonio and surrounding areas. The aquifer spans fourteen counties in Texas and lies within an area of strongly heterogeneous fractured rock formations known as the Balcones fault zone. The population in the city of San Antonio has increased by 11.8% over the period from 2000 to 2006 (U.S. Census Bureau website, 1990 and 2000). In 2008, San Antonio was ranked fifth for numerical population increase (U.S. Census Bureau News Release, 2009). Population and water demand is projected to continue to increase in the future. Understanding the hydrogeophysical properties of the aquifer is necessary to ensure that management plans are appropriate to guarantee the continued supply of water for the expanding population.

The effect of faulting and jointing on fluid flow paths is well documented and is significant enough to require the development of different approaches to modeling and measuring from those traditionally used to treat porous nonfractured media (Berkowitz 2002). Although fractures are often idealized as smooth planar features, they are in actuality rough and display self-affine fractal properties regardless of rock type. The surface roughness typically scales as a power-law (Berkowitz, 2002; Poon *et al.*, 1992; Mandelbrot *et al.*, 1984).

This thesis is written in the style of *Geophysics*.

The relationship between self-affine fractal properties at the small scale (tens of centimeters) and observations of fracture surfaces and field-scale fractures is a popular topic for research. Current theory dictates that the displacements and lengths for most fracture systems scale as power law distributions that do not exhibit a characteristic length scale (*Bonnet et al.*, 2001). The heterogeneous nature of fracture systems with power law scaling behavior and the extent of fracture connectivity in rock require careful consideration of the model parameters needed to describe fluid movement.

The use of transient controlled-source electromagnetics allows one to image geoelectrical structure at depth. The flow of electrical current in geologic media follows pathways that are spatially correlated with the flow paths of water, motivating the use of controlled-source electromagnetics (CSEM) to investigate the extent of fracturing in the Edwards aquifer. A helicopter CSEM survey conducted in the Seco Creek area by the USGS was designed to gather data over the three components of the aquifer system – the catchment, the area of recharge, and the artesian zone. Helicopter electromagnetic (HEM) surveys provide a way to simultaneously collect data over multiple frequencies along straight survey lines of great length without the inconveniences of rough terrain or vegetation that negatively affect the efficiency of ground-based data acquisition. HEM data sets have been used to examine a variety of geologic and environmental issues (i.e., *Multala et al.*, 1996; *Cook and Kilty*, 1992; *Finn et al.*, 2001).

Accommodating the accepted “roughness”, or heterogeneity, of fracture distributions is accomplished by generalizing the standard Maxwell diffusion equations to include a fractional spatial derivative (*Weiss and Everett ,2007*). The research presented here consists of two parts: (1) a prefatory analysis of transient controlled-source electromagnetic response for layered models containing a “rough layer” described by a length-scale dependent electrical conductivity and for which the assignment of a roughness parameter β_v is introduced to describe a fractured layer at depth; and (2) an analysis of the Seco Creek HEM data set in terms of a lateral roughness parameter β_H that varies with frequency and with location along the flight line. The new analysis of the HEM data set leads to fresh insights about the subsurface fracture distribution within the aquifer. Both parts (1) and (2) are aimed at direct detection of fracture properties using controlled-source electromagnetic methods. Future work on multi-dimensional EM modeling is beyond the scope of this thesis but is needed to explore the connection between β_v and β_H and to develop a single theory that accounts for both depth-dependent and laterally variable geological roughness.

The complexity and extent of small- and large-scale faulting in the Balcones fault zone makes it difficult to detect faults with small offset using surficial geological mapping techniques. The fine details of many of the mapped faults are poorly constrained (*Blome et al.*, 1994).

Further, there is very little reliable information on the geometry of buried faults within the water transmissivity region. As a result, it is known that faults and fractures can act as either conduits or as locally impermeable regions (*Ferrill et al.*, 2004). The behavior of faults and fractures depends on displacement, depth, and also the clay content that develops by communitation associated with the movement along the rough-walled fault zone. Quantitative analysis of transient controlled-source electromagnetics data permits probing of fractured layers and inferences about the extent and spatial distribution of fracturing. CSEM data therefore can help to answer questions about the quantity, quality, and mechanisms of water transport within the Edwards aquifer.

1.2 Objectives

The geology of the Edwards aquifer has been the focus of geological investigations for many years, with early papers dating back to 1961. Several United States Geological Survey (USGS) surveys have been conducted in the Edwards aquifer to map faults and constrain the properties of geological units (e.g. *Small and Clark, 2000*). A helicopter controlled-source electromagnetics (HEM) data set acquired over the Seco Creek area in Medina and Uvalde Counties, TX is used in this thesis and is available to the public online (*Smith et al., 2003*). The significance of the Edwards aquifer as a water resource to the growing population of San Antonio and the complexity of its depositional and diagenetic history motivated the analysis of the data presented here.

Section II presents a discussion of the geology of the area, including descriptions of the depositional environment, stratigraphy, and porosity and permeability of the aquifer units.

The theory for the transient controlled-source electromagnetic response over a plane layered earth model is summarized in Section III.

Section IV is devoted to a discussion of altering the homogeneous plane layered earth forward algorithm to model the case of a layered earth which contains a parameter β_v in each layer. The parameter β_v describes the length-scale dependence of the electrical conductivity. The extension of the classical modeling is performed with a view toward

detecting fractured layers at depth which follow a power-law distribution, as presented by Bonnet *et al.* (2001), Bour and Davy (1997) and others.

In Section V, a brief literature review of previous HEM studies is provided to explore the versatility of applications of the HEM survey technique. In the Edwards aquifer data set, the parameter β_H is introduced as the slope of the apparent resistivity wavenumber spectrum derived from windowed Fourier transforms of the HEM flight-line data. The parameter β_H is used to quantify lateral roughness. Along-line variations of the β_H parameter are interpreted in terms of lateral changes in the length-scaling properties of fractures. The HEM data set consists of six frequencies ranging from 400 – 100,000 Hz. Responses at lower frequencies correlate with structure at greater depths and responses to higher frequencies correlate with shallower structure.

Section VI consists of processed data analysis. 18 survey lines are analyzed to determine the change in value of β_H with distance along the line. Methods of processing the data are presented. Maps of β_H for the area covered by the survey lines are produced. The maps allow one to observe trends in length-scale dependence at a variety of depths within the aquifer. Correlations with the region's geology are discussed.

Conclusions and suggested areas for future work are presented in Section VII.

II. GEOLOGY AND HYDROLOGY OF THE EDWARDS AQUIFER

2.1 The Edwards Aquifer and Surrounding Geology

The Edwards aquifer lies in the Balcones fault zone and consists of highly permeable and porous limestone rocks deposited in the early Cretaceous. Stratigraphically, it is confined at its base by the upper bed of the less permeable Glen Rose Limestone and at its top by the Upper Cretaceous Del Rio Clay, the Buda Limestone, the Eagle Ford Group, the Anacacho Limestone, and the Escondido Formation. In some places, the Escondido Formation is overlain by the Quaternary Leona Formation. Hydrologically, the aquifer is bounded at the north at the edge of the Edwards group by the Edwards Plateau and in the south and east by the “bad water” line, where the concentration of dissolved solids increases (*Maclay and Small, 1986; Schultz, 2006; Deike, 1991*). Recharge in the aquifer occurs as meteoric water enters the network of faults and fractures in the recharge zone to the north of the Edwards aquifer rocks, as seepage from streams in the Hill Country occurs, and as inflow and upper leakage from the adjacent Trinity aquifer (*Barker and Ardis, 1996*).

2.2 Depositional Environment of Edwards Group and Associated Sedimentary Rock Units

The upper layer of the Lower Cretaceous Glen Rose Limestone is composed of interbedded limestone and marl and forms the base of the Edwards aquifer. Deposited in a calm shallow marine environment, reef structures developed in water with lower than normal levels of salinity. During the time when the Edwards group was deposited, the Stuart City Reef, composed of rudists, corals, and algae, acted as a barrier between the shallow sea depositional environment covering the interior of Texas and the deeper waters of the ancestral Gulf of Mexico (*Abbot, 1975; Barker and Ardis, 1996*).

The sediments deposited during the early Cretaceous to form the rocks of the Edwards aquifer and associated units were deposited in shallow water over the relatively flat Comanche shelf (*Rose, 1972*), which was surrounded by two depositional basins: the Maverick basin in the southwest, and the North Texas-Tyler basin in the northeast. The northern border of the Maverick basin consists of the Devils River Trend, a ridge of bioclastic sediments. The Edwards aquifer was deposited over the centrally located San Marcos platform to the southeast of the Comanche shelf, which is adjacent to the Stuart City Reef (Figure 2.1) (*Abbot, 1975*).

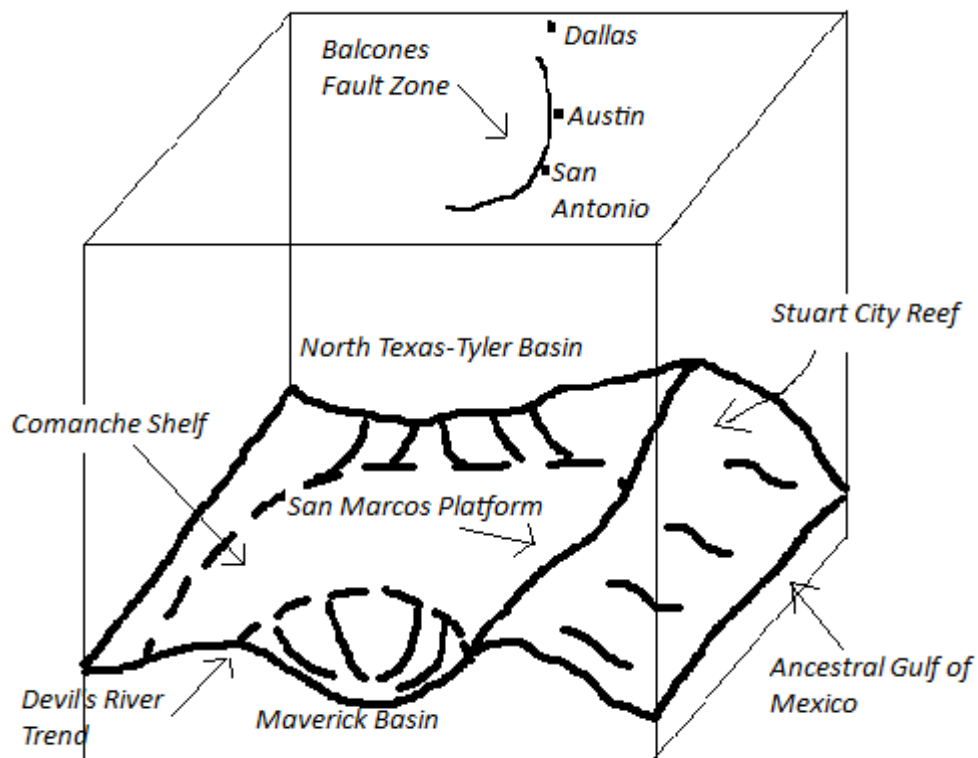


Figure 2.1: Representation of depositional geography during the Lower Cretaceous with location of cities indicated for reference (adapted from *Abbot*, 1975)

The Edwards aquifer rocks were deposited in an upward-shallowing sequence with four distinct cycle types, resulting in textural and compositional variations in the formations. The four cycle types and their associated properties are detailed in Table 2.1.

Table 2.1: Description of depositional cycle and associated material properties for the Edwards aquifer rocks (*Hovorka et al.*, 1994).

Cycle	Description
Subtidal, low-energy	High organic and argillaceous content, wispy laminated wackestones and packstones, mud-dominated packstones
Subtidal, low- to high-energy	Mud-rich rock formed in low energy environment grades up to higher energy, grainy facies indicative of upward shallowing. Grain-dominated packstone where sediments were held in place by sea grass, coarser grainstone with evidence of crossbedding or lamination in high-energy environments
Hypersaline	Pseudomorphs of gypsum are common and easily recognizable as many crystals exhibit twinning or have formed at unique angles
Subtidal low-energy to intertidal/supratidal	Subtidal facies are mostly dolomites with fine texture. Supratidal facies have been exposed and have been complexly altered after deposition

The Del Rio Clay is a terrigenous unit that formed as the San Marcos platform was uplifted. It was deposited over the Georgetown Limestone Formation, which was in turn deposited after the uplift and erosion of the Person Formation. Although the Georgetown Formation was deposited after the rest of the Edwards group, it is traditionally included as a member of the aquifer by well loggers (*Maclay and Small*, 1986). Together, the Georgetown Formation and the Edwards Group comprise the Devils River Formation (*Small* 1986). The Del Rio Clay is composed partially of ash from volcanic eruptions on the west coast of the continent and partially of local sediments (*The Edwards Aquifer Website*, 2005-2009). Limestone units above the Del Rio Clay were deposited as the San Marcos platform was once again covered by shallow sea.

2.3 Balcones Fault Zone

The Balcones fault zone follows the trend of the Paleozoic Ouachita fault zone beneath it. Movement in the Balcones fault zone occurred in the Late Oligocene to Early Miocene as the Gulf of Mexico subsided (*Collins, 1987*). The fault zone has a “horst-and-graben” style of faulting with an en echelon pattern in the study area for this thesis (*Collins, 1987*). Total displacement over the aquifer ranges from ~275 to ~366 meters, increasing the hydraulic flow gradient (*Barker and Ardis, 1996; Ferrill et al., 2004*). The faults are mostly northeast with downward displacement in the southeast direction. There are a few northeast to southwest cross faults. In some places, throw along the major faults is as much as 183 m (*Collins, 1995*), which approaches or exceeds the thickness of the Edwards group rocks, creating local barriers to north-to-south flow and conduits along the fault trace, causing the water to move from the north to the northeastern part of the aquifer (*Ferrill et al., 2004; Pantea and Cole, 2004*). Zones of well-connected smaller faults and some joints are known to surround the major faults in the Balcones fault zone. Although fractured strata in the Edwards aquifer is not well-documented, it is common to have larger damage zones adjacent to larger faults with the extent and connectivity of fractures diminishing with distance from the fault (*Collins, 1995*). In some sections of the aquifer, relay ramp structures connect en echelon faults such that the aquifer layers are continuous (*Hovorka et al., 1994*).

The north to northeastward movement of water in the Balcones fault zone has created a definite divide between the aquifer-quality “fresh” water and the more saline water that lies to the south, which has dissolved solid concentrations ranging from 700 to 8,000 mg/L (Deike, 1991). The boundary is commonly referred to as the bad water line. A sketch of the Balcones fault zone with the bad-water line marked is provided in Figure 2.3.1.

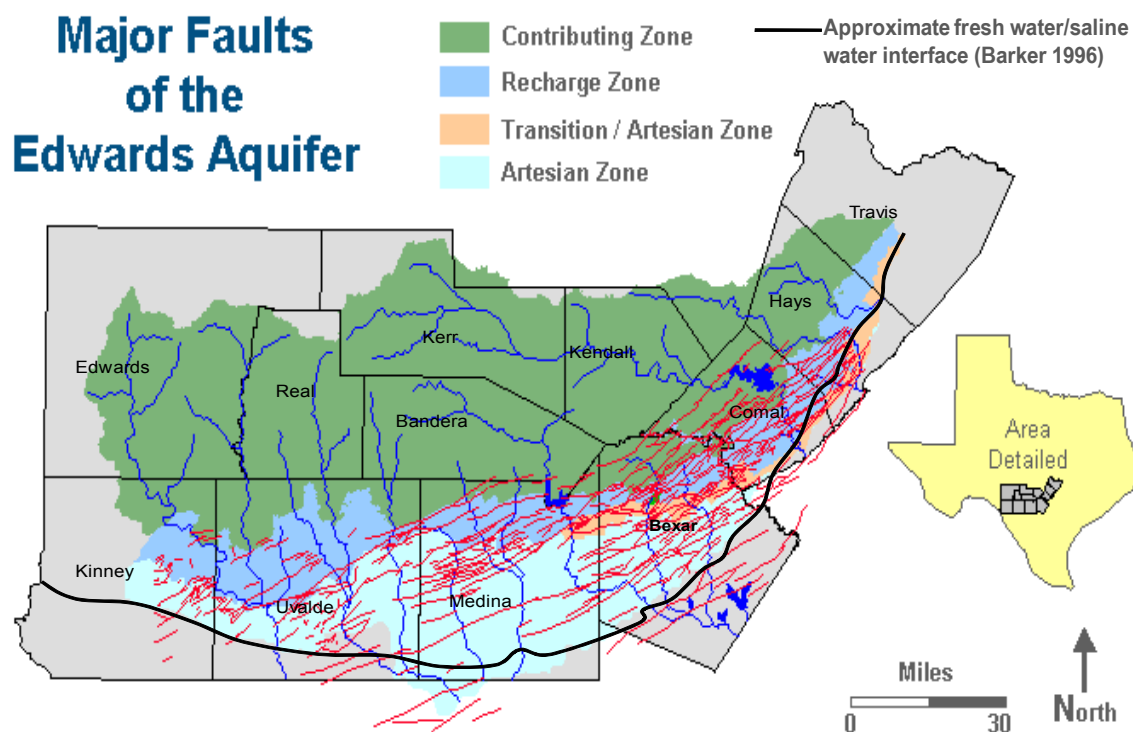


Figure 2.2: Map of Edwards aquifer area with counties labeled. Red lines indicate mapped faults. The bad water line is marked in black (adapted from Collins and Hovorka, 1997; Deike, 1991)

2.4 Stratigraphy and Porosity

Figure 2.2 shows several regions of interest in the Edwards aquifer system. The focus area for this thesis covers the contributing zone, the recharge zone, and the artesian zone. The stratigraphy for each zone is well known. On the geologic map (Plate 1), the Upper Glen Rose Formation is exposed over the contributing zone with localized remnants of the Lower Devils River Formation. The Lower Devils River Formation has not been eroded on the downthrown side of the Woodard Cave Fault, where the area of recharge is marked. To the south, the aquifer is confined by Cretaceous rocks belonging to (from top of Edwards Group to surface) the Del Rio Formation, the Buda Formation, the Eagle Ford Formation, the Austin Group, the Anacacho Limestone, the Escondido Limestone, Quaternary and Upper Tertiary Uvalde Gravel, and the Pleistocene Leona Formation. A description of each unit is given in Tables 2.2 and 2.3.

Table 2.2: Description of the units within the Devils River Formation. The units may be further subdivided to account for variation in texture and calcite content (*Small and Clark, 2000*).

DEVILS RIVER FORMATION			
Lithostratigraphic Unit		Thickness (m)	Characteristics
Georgetown Formation		0-6	Marly limestone with brachiopods
Edwards Group	Person Formation	26-37	At base, argillaceous mudstone. Above, dolomitic biomicrite and leached, collapsed breccia. On top, grading from mudstones to packstones to miliolid grainstone.
	Kainer Formation	79-98	At base, fossiliferous mudstones and wackestones with extensive burrows. Above this, dolomitic mudstones. On top, crystalline limestones.

Table 2.3: Description of the units confining the Edwards aquifer (*Small and Clark, 2000*).

UPPER CONFINING UNITS			
Lithostratigraphic Unit		Thickness (m)	Characteristics
Pleistocene Leona Formation		up to 20	Sands and gravels
Quaternary and Upper Tertiary Uvalde Gravel		variable	Gravels
Upper Cretaceous	Escondido Formation	91	Gray sandstone and shale
	Anacacho Limestone	73 to 122	Brown fossiliferous limestone
	Austin Group	69 to 107	Light colored chalky to marly fossiliferous limestone
	Eagle Ford Group	9 to 15	Brown shale and argillaceous limestone
	Buda Limestone	12 to 15	Light colored dense mudstone
	Del Rio clay	12 to 15	Blue-green to yellow-brown clay

Porosity in the Edwards aquifer is both fabric selective and not fabric selective. The term “fabric selective” refers to porosity that is related to the texture and structure, referred to as fabric elements, of the initially deposited sediment particles and the particles (or crystals) that have resulted from diagenesis. Porosity that is not fabric selective is independent of fabric elements (*Choquette and Pray, 1970*). In a study of thin sections and core samples by Hovorka *et al.* (1994) types of fabric selective porosity seen in the aquifer are: intergranular (in grainstones), intercrystalline (in dolostone), intergranular and intercrystalline porosity that has been enhanced by dissolution, and burrowing, which may or may not be fabric selective. The term interparticle may be used in place of intergranular and intercrystalline to collectively describe the two types of porosity as their petrophysical properties are similar (*Lucia, 1995*). Not fabric selective types of porosity found in the aquifer are fracture porosity, which is enhanced in some layers by dissolution, cavernous porosity, vuggy porosity, and breccia porosity (*Small and Clark, 2000; Hovorka et al., 1994; Lucia, 1995*).

Porosity and permeability are affected by the extent of dolomitization and dedolomitization in carbonate rocks. The distribution of pore sizes in the rocks can be determined by grain or crystal size and mud content, amount of sorting, and interparticle porosity when vugs are not present (*Lucia, 1995*). The rocks in the Edwards aquifer have undergone both dolomitization and, in some areas, subsequent dedolomitization. The process of dolomitization usually serves to increase or maintain the permeability of the rocks while decreasing the porosity as dolomite crystals grow (*Lucia, 1995*).

During the process of dedolomitization, the dolomite crystals are replaced by calcite as calcite-rich, magnesium-poor meteoric water flows through dolomitized rocks. A comparison of a core sample taken from the fresh water section of the Edwards aquifer to a nearby core sample taken where the bad water line crosses showed vast differences in calcite content and porosity. Taken in the fresh water zone, the low value of core recovery for the Selma well (65%) is attributed to the presence of cavernous porosity as samples retrieved from the well showed evidence of rounding of particles from dissolution. Geochemical analysis showed that percentages of calcite, indicative of dedolomitization, ranged from 50-100% relative weight of inorganic components at almost every level in the Devils River Formation (*Deike, 1991*). Calcite content decreased significantly in the much less cavernous underlying Glen Rose Formation. The Randolph well was drilled into the bad water region. With the exception of some calcite-dominant biomicrite and biosparite sections, calcite content was significantly lower than dolomite content, which ranged from 40-98% relative weight in most layers (*Deike, 1991*). The large percentage of dolomite in the core sample from the bad water region suggests that dedolomitization has not occurred, in agreement with evidence that water in the aquifer rocks flows eastward through large vuggy pore spaces and fracture or faulting networks instead of south, toward the Gulf of Mexico, and into the bad water zone. The Selma and Randolph holes are eastward of the thesis study area, but the depth of the wells ensures that all facies of the Edwards aquifer were tested and the results can be extended to the study area.

Crystals of gypsum grew in the hypersaline cycle of deposition. Gypsum was commonly retrieved in the Randolph well core. In some sections, it averaged at 25% by weight of total sample. In the Selma core, gypsum was rarely recovered (*Deike, 1991*). The relationship between porosity changes and dissolution of gypsum by calcite-rich meteoric water is complex. In some locations, calcite cement is deposited, reducing porosity and permeability. In other places where gypsum is dissolved and cavernous or vug porosity is evident, porosity and permeability are greatly increased. It is thought that the rate of dissolution of gypsum and the order in which it occurs with regards to calcite contributes to the increase or decrease in porosity (*Hovorka et al., 1994*). For further discussion on the topic of relative rates of dissolution, precipitation, and flow in fractured carbonates, the reader is referred to Singurindy and Berkowitz (2003).

2.5 Power-law Scaling of Fractures

It is generally accepted that many fracture systems follow a power-law distribution of the form

$$n(l) \sim \alpha l^{-a} \quad (2.1)$$

where $n(l) dl$ is the number of faults in the size range $[l, l + dl]$. The exponent a describes the ratio of connected to unconnected faults, α is a proportionality constant, and l represents some fractal property, such as length or displacement (*Bour and Davy, 1997; Bonnet et al., 2001; Cladouhos and Marrett, 1996*). Values of a usually range from 1 to 3. The existence of many mapped faults with depths that exceed the thickness of the Edwards group suggests that the depositional and compositional differences between stratigraphic layers are insignificant when considering the mechanical properties of the rocks. For thick stratigraphic columns of rock where mechanical properties are consistent throughout the unit or units, power-law distributions are common and have been detected in studies of massive units of sedimentary rocks (*Berkowitz, 2002*), justifying the power-law treatment of the fractures in the Edwards aquifer.

The ability of fluids to flow through units with power-law distribution is determined by percolation theory, wherein the connectivity of fractures is critical. Percolation theory usually uses the power-law relationship

$$A \sim \alpha (N - N_c)^{-x} \quad (2.2)$$

where A is some quantity that has been observed, such as conductivity, α is a

proportionality constant, N is the total number of fractures in the study area, N_c is the critical number of fractures at the threshold where the system becomes connected so that fluid can move from one side of the study area to the other through some part of the network, and the exponent $-X$ is specifically related to quantity A (Berkowitz, 2002). Areas with fracturing that has resulted from stress, such as the Edwards aquifer, are naturally close to or above the percolation threshold so that water can move easily through the strata (Guéguen *et al.*, 1991). Rates of hydraulic transmissivity in the Edwards aquifer are very high (ranging from 18580 m²/d to 185800 m²/d in most places), clearly indicating that the fracture network is extensively connected (Deike, 1991).

III. CLASSICAL INTERPRETATION OF CSEM DATA

3.1 Theory

This thesis is concerned with controlled-source electromagnetic (CSEM) geophysical probing of fractured rock aquifers. It is well established that CSEM data are sensitive to the electrical conductivity distribution, i.e. the measurements provide an indication of the subsurface geoelectric structure. The problem of interpretation is to relate the inferred electrical conductivity to hydrogeological parameters of interest such as fracture distribution. Here, an attempt is made to provide such an interpretation. The basic approach is to extend the classical theory of EM induction to the case of a layered, rough geoelectrical medium. A rough geoelectric layer is defined as one in which electrical conductivity obeys power-law length-scaling. In that case, electrical conductivity can be represented by a single roughness parameter, namely the power-law exponent. The rough layer is hypothesized to represent a fractured medium in which the fractures are also power-law distributed with the same exponent as that of the electrical conductivity.

In the setup for the inductive CSEM method considered here, a closed loop of wire is employed as the transmitter. In land-based surveys, the transmitter loop is laid out on the ground and a second receiver loop is placed some distance away at slight elevation above the surface. The receiver loop is employed to detect the magnetic field arising from eddy current induction in the ground. In some airborne surveys, the transmitter and receiver

loops are separated by a fixed distance and housed in a bird (often with other equipment for sensing elevation, total magnetic field of the earth, and position). The bird is towed behind a helicopter. In other common airborne systems, the transmitter loop is wrapped around a helicopter or fixed wing aircraft and the receiver loop is towed behind the aircraft.

In response to a time variation of current flowing in the transmitter loop, an eddy current vortex forms within the conductive ground. The electromagnetic vortex has the same shape and time evolution as a hydrodynamic vortex, such as a smoke ring. In both cases, the vortex propagates by self-induction described by the Biot-Savart law. The CSEM receiver detects the magnetic field that is generated by the subsurface current vortex. Computation of the electromagnetic loop response over a prescribed geoelectrical model generally assumes the classical Gaussian shape for the eddy current vortex. The Gaussian shape arises as a consequence of the traditional pre-Maxwell diffusion equations containing integer spatial and time derivatives (Figure 3.1). In this section, we review the classical solutions to the pre-Maxwell equations for a ground-based loop deployed over a plane-layered Earth characterized by piecewise uniform homogeneous conductivity. In subsequent sections, we extend the analysis to include rough layers in which the conductivity of each layer may be length-scale dependent.

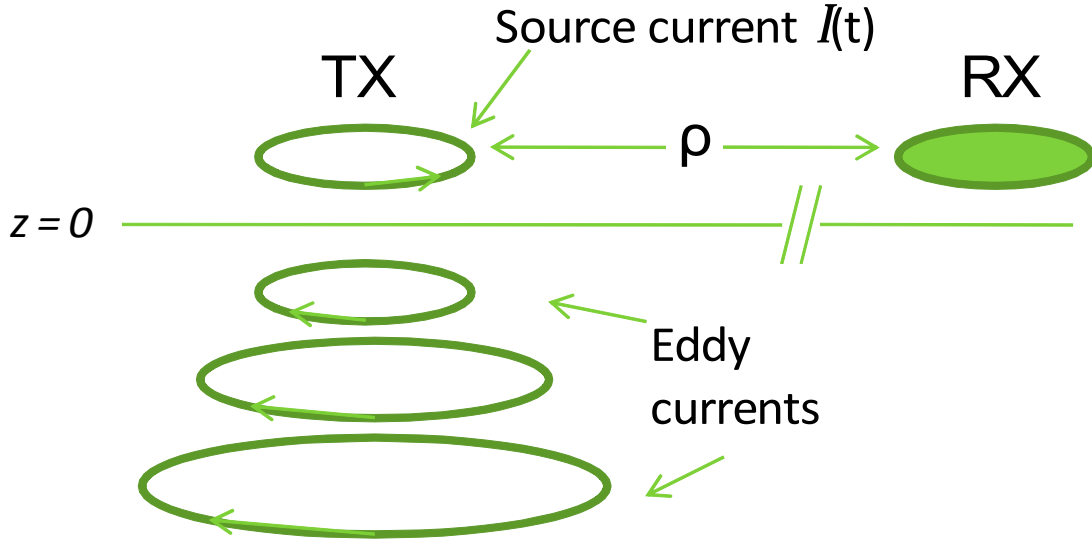


Figure 3.1: Schematic of eddy current diffusion in the subsurface in a ground-based loop configuration

The analytical form of the electromagnetic loop response for a piecewise-continuous (classical) half-space has been derived by many authors, including Ryu *et al.* (1970). The half-space solution to a layered-earth model with $N-1$ layers over an infinite half-space (see Figure 3.2), involves a Hankel transform with a kernel that is expressed in terms of a recursion relationship that describes the layer impedances. Following the derivation in Ryu *et al.* (1970), for a harmonic transmitter frequency ω , current I and loop radius a , the expression for the secondary electrical field, $E_s(\rho, z)$, at source-receiver (TX-RX) separation distance ρ is

$$E_s(\rho, \omega) = -i\omega\mu_0 I a \int_0^{\infty} \exp(-\gamma_0 z) / \gamma_0 \cdot Z^l / (Z_0 + Z^l) \cdot J_1(\lambda a) J_1(\lambda \rho) \cdot \lambda d\lambda, \quad (3.1)$$

where J_1 is the first-order Bessel function. Here it is assumed that the TX loop is lying on the ground surface $z=0$, while the RX loop is located in the air at height z above the surface. The formulae must be adjusted to accommodate the distance between the ground and the TX loop in the airborne survey. The propagation constant within layer i is $\gamma_i = (\lambda^2 + i\omega\mu_0\sigma_i)^{1/2}$ for $i=1, \dots, N$, such that for the overlying air layer $\gamma_0 = \lambda$. The characteristic impedance of the i -th layer is $Z_i = -i\omega\mu_0/\gamma_i$ while the input impedance Z^i to the i -th layer is given by the recursion relation

$$Z^i = Z_i [Z^{i+1} + Z_i \tanh(\gamma_i h_i)] / [Z_i + Z^{i+1} \tanh(\gamma_i h_i)] . \quad (3.2)$$

The characteristic impedance of the terminating half-space is $Z^N = Z_N$, so that the input impedance Z^1 at the surface can be computed by recursion, using equation (3.2), upward through the stack of layers. The vertical magnetic field $H_z(\rho)$ at the surface $z=0$ is then readily found using Faraday's law

$$H_z(\rho, \omega) = i/\omega\mu_0 \partial/\partial\rho [\rho E] , \quad (3.3)$$

where the total electric field $E = E_S + E_P$ is given by the secondary electric field in equation (3.1) plus the well-known primary electric field E_P of a loop in free space.

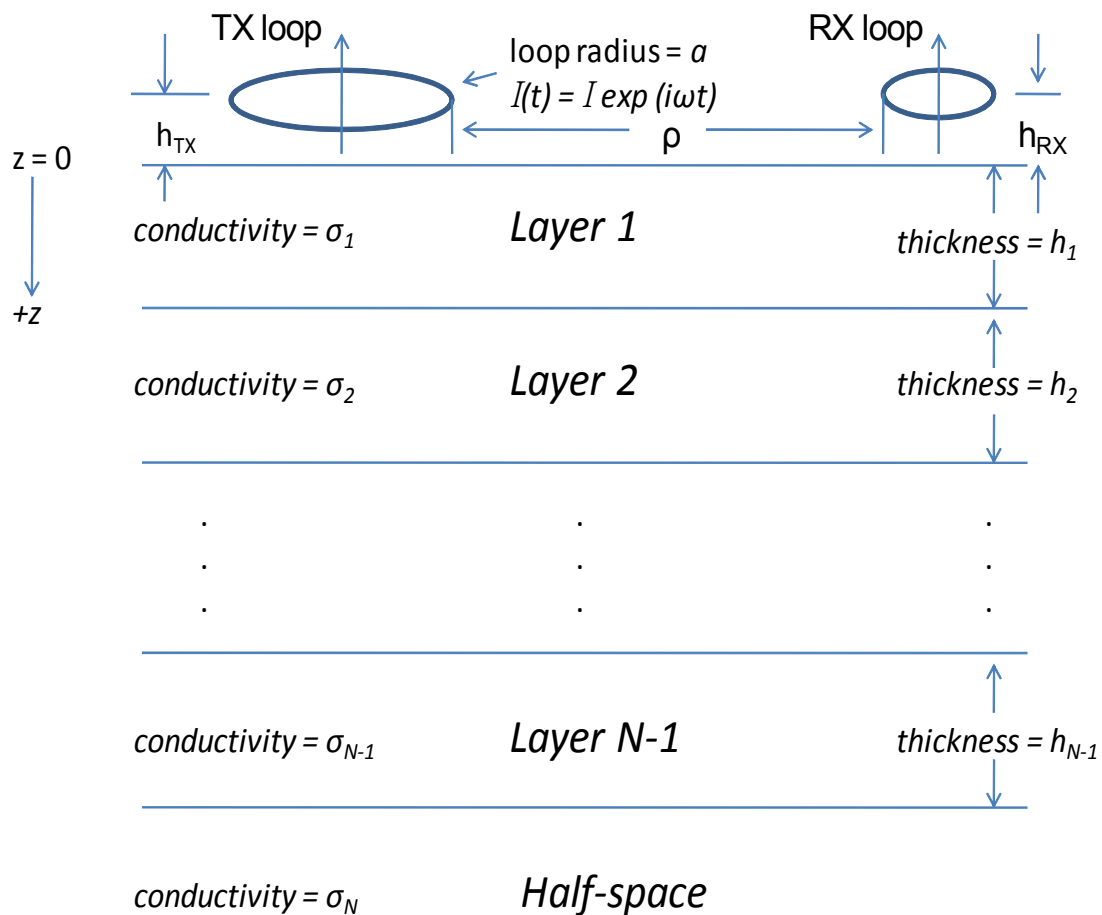


Figure 3.2: Schematic of plane-layered homogeneous earth with heights h_{TX} and h_{RX} labeled to represent the elevation of the HEM equipment.

3.2 Limitations of Classical Theory

Fractures in the Edwards aquifer are thought to have a power-law scaling relationship. Assuming that the fracture distribution is spatially correlated with electrical conductivity, such that both possess the same power-law exponent, the classical assumption of smooth homogeneous layers for this study area breaks down. The roughness of layers at depth produces an electromagnetic response that is non-classical. If sounding data from a fractured aquifer are to be modeled, using the equivalent classical response would involve a very large number of thin homogeneous layers. Such an interpretation of smooth homogeneous layering is not supported by the stratigraphy of the aquifer as discussed in Section II. A much more compact representation of the data is available using the rough-geology extension of the classical CSEM theory.

IV. INHOMOGENEOUS “ROUGH” PLANE LAYERED CASE AND MODELS

4.1 Extending Homogeneous Plane Layered Theory to the Inhomogeneous Plane Layered Case

This section is concerned with modeling the electromagnetic response of a medium containing a power-law distribution of fractures, as described in Section II for the sedimentary rocks associated with the Edwards group. It is necessary to adjust the theory presented in Section III to accommodate length-scale dependence, or “roughness”, in the conductive layers. A roughness parameter, β_v , such that $0 \leq \beta_v < 1$, is introduced in Equations (3.1 – 3.3) to adapt the classical theory to the case where roughness exists in one or more layers at depth. The roughness parameter β_v is essentially the power-law exponent of length-scaling. Larger values of β_v appear when long-range spatial correlations dominate. Smaller values of β_v indicate that shorter-range spatial correlations are more important.

The incorporation of β_v into the plane-layered electromagnetic response is developed by generalizing the solution of the time-fractional Maxwell diffusion equation for the rough half-space, which appears in Weiss and Everett (2007) and Everett (2009). The extension of the rough half-space solution to a layered model uses the identical recursion relationship as in (3.2), except with a simple change from $(i\omega) \rightarrow (i\omega)^{1-\beta_v}$ in the expressions for characteristic impedance:

$$\gamma_i \rightarrow [\lambda^2 + (i\omega)^{1-\beta_{v_i}} \mu_0 \sigma_i]^{1/2} \quad (4.1)$$

where β_{v_i} is the roughness parameter of the i -th layer. Note that the classical layered earth response of Ryu *et al.* (1970) is recovered when $\beta_{v_i} = 0$, for all $i = 1, \dots, N$.

A schematic view of the relationship between spatial roughness β_v and the length-scale dependence of electrical conductivity may be found in Figure 4.1. It is assumed that the fracture density obeys the same power-law scaling as electrical conductivity. As the slope increases, the structure becomes increasingly rough and the value of β_v increases.

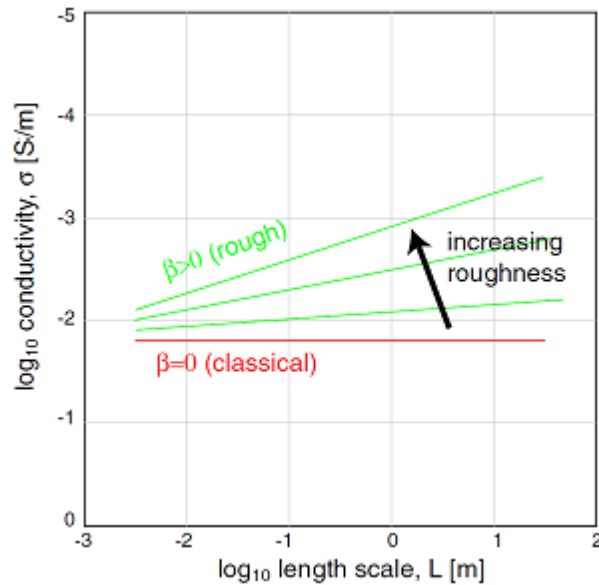


Figure 4.1: Generalized electrical conductivity with power law dependence on length scale L . The power law exponent is the roughness parameter β_v .

4.2 Modeling

A *fortran* code was developed to evaluate the step-off transient electromagnetic loop response for multi-layered, rough electrical conductivity models that are relevant to fractured-rock aquifer characterization. The step-off transient response is found by performing a standard cosine transform (Chave 1983) of the frequency-domain response $H_z(\rho, \omega)$ in equation (3.3) calculated at several frequencies and then splined to produce a continuous spectrum spanning several decades of frequency. The *fortran* code was validated by checks against previously published curves for the classical ($\beta_v=0$) multi-layered case in Ryu *et al.* (1970) and the rough half-space ($N=1$) case in Everett (2009).

Four different models relevant to the exploration of fractured-rock aquifers were developed and analyzed to test the ability of the new CSEM analysis method to detect and characterize a buried rough layer. Conductivities for the common sedimentary materials used in the model aquifer layers are shown in Table 4.1. The parameter value $\beta_v > 0$ presumably indicates the presence of a fractured layer. In actuality, any spatially correlated heterogeneity caused by lithological, water content or other variations can give rise to a β_v value that is different from zero. For the classical case, which is assumed to be a homogeneous intact rock layer, we have the null roughness value $\beta_v=0$. In the table, the change of conductivity resulting from fracturing is accommodated by increasing the β_v parameter. For the models based on the data presented, both the conductivity and the value of β_v may be changed to reflect the electrical properties of the fractured layer.

Table 4.1: Conductivities of common sedimentary aquifer rocks.

material	conductivity, σ (S/m)	roughness, β_v
intact shale	0.1	$\beta_v=0$
intact dry sandstone	0.001	$\beta_v=0$
intact wet sandstone	0.1	$\beta_v=0$
fractured rock	same value as intact rock	$\beta_v>0$

For each model, an electrical conductivity is assigned to two layers overlying an infinite half-space. The step-off transient controlled-source electromagnetic loop-loop response is plotted in log-log space with RX voltage v. time. These data may be collected using instruments such as the Geonics TEM47. For the TEM47, a current with a very fast turn-off time (on the order of $0.5 \mu\text{s}$) is generated and data is sampled at 20 time gates, spaced $142.55 \mu\text{s}$ apart, as the current diminishes (*GEONICS website*, 2009).

Log-log plots show the decay of the induced magnetic field in terms of the voltage at the receiver coil over two decades of time. The cusp for each curve occurs where the eddy currents triggered by the current in the TX coil pass beneath the RX coil, causing a change in sign. This point is called the zero-crossing time.

The response for Model 1 is pictured in Figure 4.2. For this model, conductivity is uniform through the two layers and half-space, but the second layer is assigned a value of β_v that is set to four different values, ranging from the classical case where $\beta_v=0$

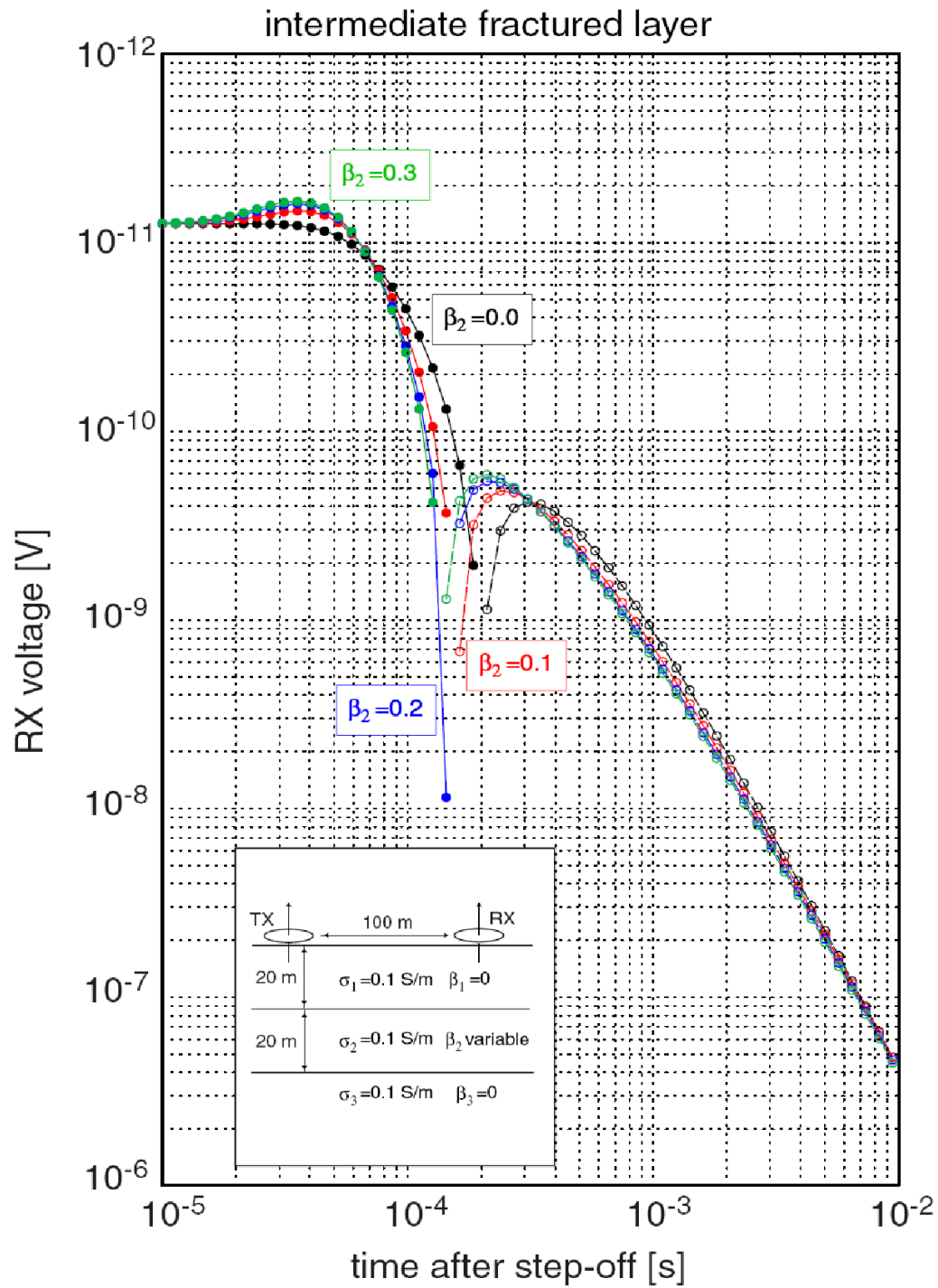


Figure 4.2: TEM47 response curves for a 3-layer model with conductivity $\sigma=0.1 \text{ S/m}$ appropriate for shale or wet sandstone. The models contain a rough intermediate layer characterized by $\beta_v \geq 0$.

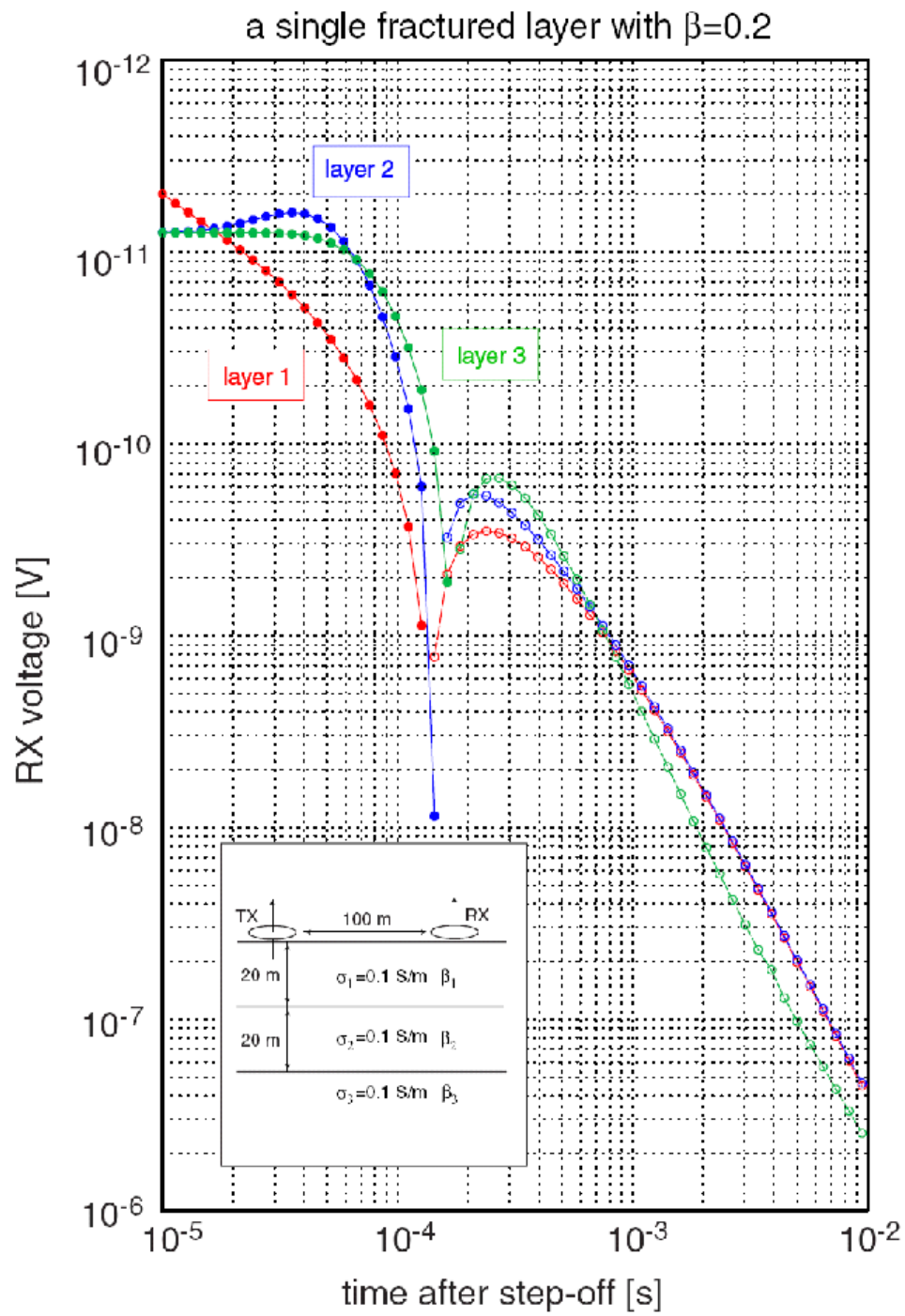


Figure 4.3: TEM47 response for sensitivity to depth, tested by adjusting the depth of the fractured layer.

to an inhomogeneous case where $\beta_v = 0.2$. The slight change from $\beta_v = 0$ to $\beta_v = 0.1$ shows a remarkable change in the shape of the curve for the electromagnetic response. Higher values of β_v also show deviation from each other and the classical case. This shows that a rough layer may be detected using the TEM47 instrument.

Figure 4.3 is the response from Model 2, where the sensitivity to depth of a heterogeneous layer is tested by applying a continuous conductivity to all layers while placing a fractured layer with $\beta_v=0.2$ at the surface, in the middle, and at the base of the stratigraphy to generate three distinct curves. Changing the depth to the fractured layer produces dramatic changes in the shape of the response curve.

To investigate the EM response for the case in which a resistive, fractured layer underlies a conductive layer, the intermediate layer is assigned a conductivity appropriate for dry sandstone in Model 3 (Figure 4.3). As with classical models for similar cases, the response of the rough model is insensitive to the intermediate, dry, resistive layer, even when β_v is assigned a large value of 0.5. Electromagnetic methods are inappropriate for detecting such a layer because the inductive loop source cannot generate the galvanic mode which is needed to illuminate a resistive layer. Most of the current is associated with the inductive mode and circulates in closed loops within the conductive overlying layer.

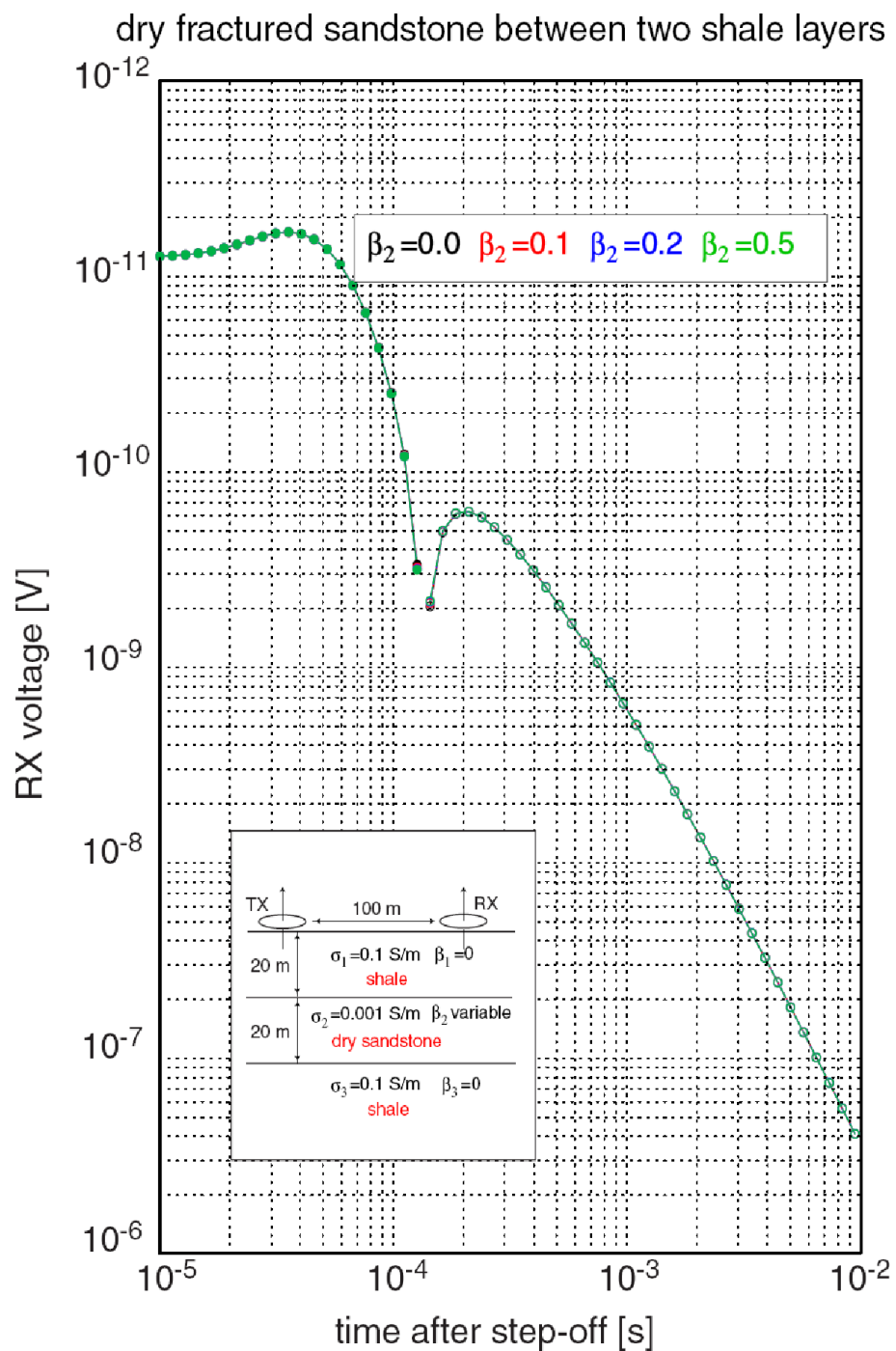


Figure 4.4: TEM47 responses for a dry, resistive sandstone sandwiched between two layers of more conductive shales.

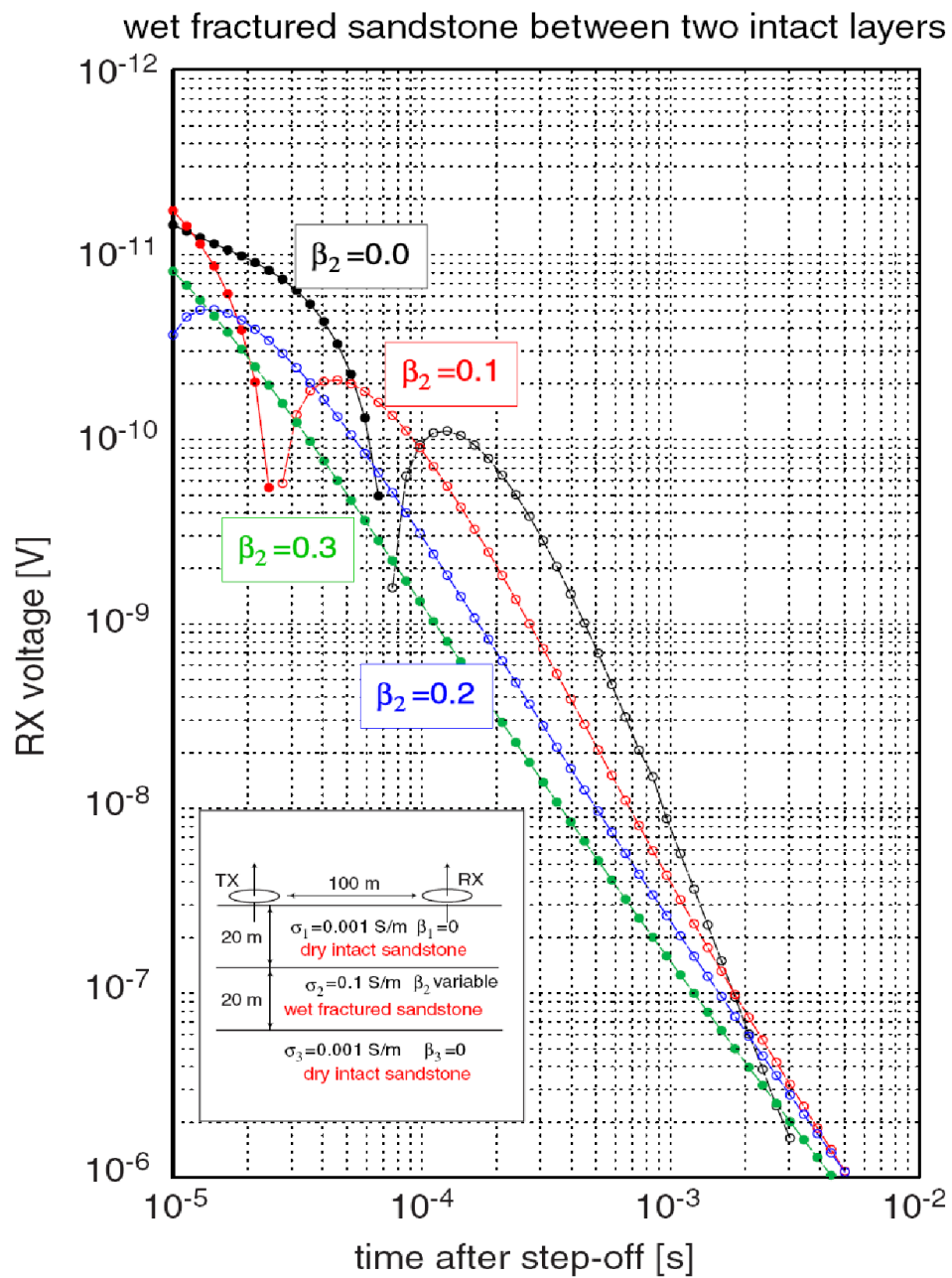


Figure 4.5: TEM47 responses for aquifer-based model with fractured middle layer.

Model 4 was developed to approximate conditions for an idealized fractured aquifer (Figure 4.4). This model suite is characterized by a layer of highly conductive fractured, wet sandstone sandwiched between two dry, resistive layers. The conductive layer is an excellent target for controlled-source electromagnetic experiments. As shown in the figure, slight changes to the value of β_v produce large changes in the shape of the electromagnetic response curves. Such changes should be easily recognized from surveys conducted in the field and can help to interpret the extent of fracturing in aquifers.

The models of 1-D soundings presented here are useful for examining the ability of CSEM models with roughness parameters to detect targeted layers. By producing more synthetic curves using the *fortran* code to model diverse geological environments, we can begin to recognize the electromagnetic response for different geological environments. In Figures 4.2, 4.3, and 4.5, it is clear that the cases with even minimally extensive fracturing produce an easily observable change in the shape of the response curve. Imaging the extent of fracturing in subsurface layers is impossible using classical interpretation models. Understanding how the models change in response to different inputs will improve the accuracy of interpreting data sets with inverse modeling.

V. HEM SURVEY

5.1 Literature Review of Airborne Electromagnetic Surveys

In cases where land-based surveys are inconvenient or impossible due to harsh or dangerous conditions, airborne electromagnetic surveys provide an alternative method of data collection.

In the Baltic Sea, mapping the thickness of sea ice is a difficult procedure. Typically, ice thickness varies from a few centimeters up to 50 meters. Ice strength also varies, based on age and extent of deformation (*Multala et al.*, 1996). In fresh water conditions, ground penetrating radar can easily image ice thickness, but in salt water the signal is rapidly attenuated. Sonar soundings, drilling, laser profilometry, and the application of Archimedes' principal are the traditional ways of measuring ice thickness. Airborne electromagnetic surveys, even with the overly simplistic parameters of sea water as a conductor and ice as a non-conductive body, returned results that allowed for easy and accurate determination of ice thickness. Results from the survey were in agreement with the thicknesses found by ground-truthing. More accurate values for sea ice conductivity to incorporate vertical salt water- or salt crystal-filled cracks in the ice will enhance the

accuracy of airborne EM surveys. Determining ice thickness and deformation allows scientists to characterize off-shore structure and will help to guarantee the safety of ships navigating icy waters (*Multala et al.*, 1996).

An airborne EM survey technique was conducted over the collapse-prone hydrothermally altered sides of Mount Rainer (*Finn et al.*, 2001). The rock was weakened when the volcano was active and a large deposit of rock on the western flank shows hydrothermal alteration that may result in a catastrophic flow of rock into a densely populated area. The EM survey was conducted to discern areas where altered rocks are covered by snow, vegetation, or unaltered rocks deposited in subsequent volcanic episodes. Altered rocks have a low resistivity due to the large pore spaces and high clay content. The fresh volcanic rocks, formed from andesitic and dacitic lavas, have a higher resistivity. The contrast in resistivity is clearly visible in the results of the EM survey and the survey results discredit previous hypotheses of a core of highly altered rocks beneath the volcano's summit. The paper was the first to study the structure of the volcano using geophysical techniques and the results, previously unattainable, demonstrate the value of the survey method (*Finn et al.*, 2001).

In a 1992 study by Cook and Kilty, the rate of recharge for an aquifer was examined using HEM techniques over an arid field site. For this survey, areas with high rates of recharge existed in sandier soils where salt leaching occurred at greater depths to produce low apparent conductivities. In other, similar surveys, it was found that higher conductivities corresponded with areas of high recharge. The conflicting results of the various studies on the relationship between recharge rate and conductivity result from differences in geological settings, but all studies show that a relationship does exist. Ground truthing provides a means for determining whether increases in apparent conductivity are inversely or directly related to increases in rate of recharge. Once the relationship is established, airborne electromagnetic surveys provide a way to interpolate between well-bores to model recharge rate for large areas (*Cook and Kilty, 1992*).

5.2 Helicopter EM Survey Details

The data set used in this thesis was collected using the Fugro RESOLVE 6 Frequency EM system (Figure 5.1). The RESOLVE system contains five coplanar TX and RX coils and one coaxial TX and RX coil at the frequencies listed in Table 5.1. The length separating the coplanar TX coils from the coplanar RX coils is 7.9 m. The coaxial TX and RX coils are 9 m apart (*Cain, 2002*).

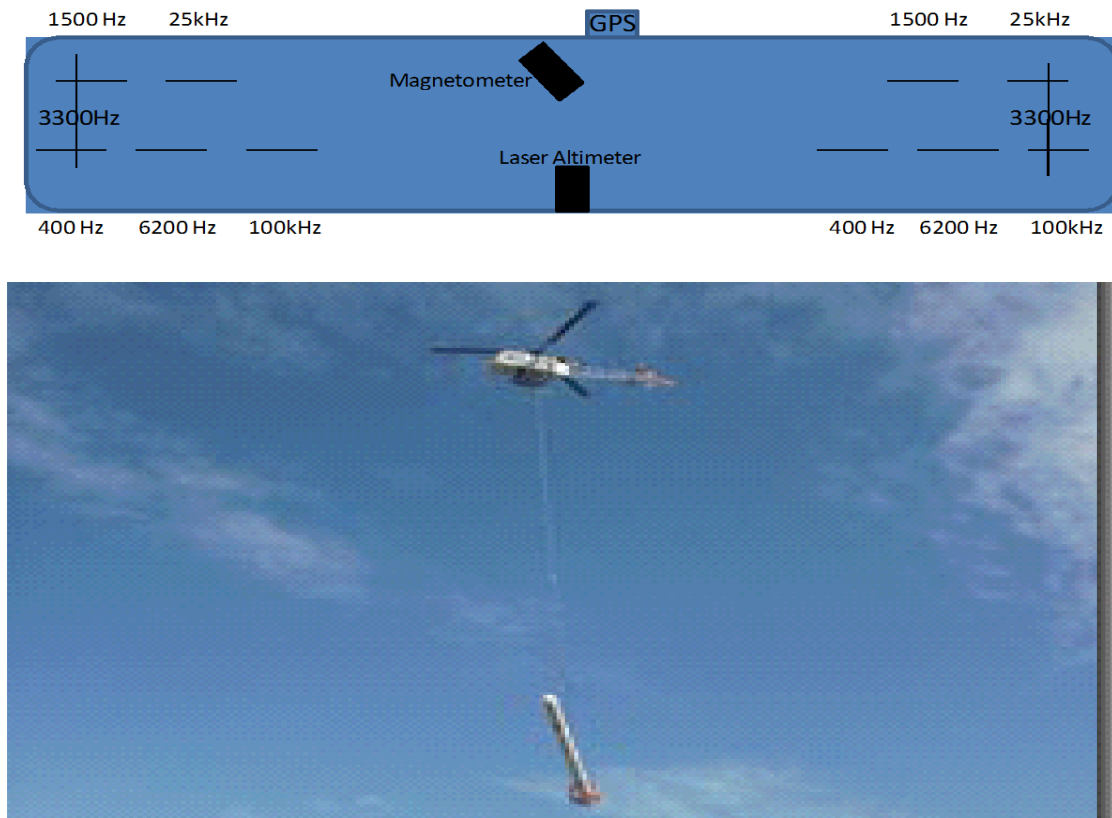


Figure 5.1: Schematic of the RESOLVE 6 System (adapted from Fugro Airborne website, 2005) and photo of system in flight.

The system also records position along the flight lines using GPS, magnetic signature with a magnetometer, and altitude with a laser altimeter.

Table 5.1: Frequencies and coil orientation for the RESOLVE 6 System. Adapted from *Smith et al.*, 2003.

COIL CONFIGURATION	Actual Frequency (Hz)	Nominal Frequency (Hz)	SENSITIVITY (ppm)
Coplanar	386	400	0.13
Coplanar	1514	1500	0.12
Coaxial	3315	3300	0.06
Coplanar	6122	6200	0.24
Coplanar	25960	25000	0.44
Coplanar	106400	100000	0.44

Different frequencies are used in the RESOLVE 6 system to probe multiple depths over the survey lines. The skin depth is a measure of the depth of penetration of EM signals into conductive ground. It is defined as the depth at which an incident plane wave attenuates to $1/e$ of its value at the Earth's surface. Estimates of skin depth, δ , can be calculated for each frequency, using the formula

$$\delta = \sqrt{2/\mu\omega\sigma} \quad (5.1)$$

where μ is permeability ($= 4\pi \times 10^{-7}$), ω is the frequency of the transmission, and σ is a representative electrical conductivity of the geological unit penetrated. Table 5.2 presents skin depths calculated for a conductivity of $\sigma = 0.01$ S/m. The table is presented for illustrative purposes and, as it is unlikely that the chosen value of conductivity is appropriate for all given layers, should be used only as a guide for penetration depth.

Table 5.2: Skin depth calculated for a conductivity of 0.01 S/m.

FREQUENCY	SKIN DEPTH
100 KHz	40 m
25 KHz	80 m
6200 Hz	160 m
3300 Hz	220 m
1500 Hz	326 m
400 Hz	631 m

The airborne electromagnetic survey was conducted over the Seco Creek area in Medina and Uvalde Counties, TX (Figure 2.2 for geographic location) and is centered on the karstic Valdina Farms sinkhole, also called Woodard Cave, which is in the Seco Creek drainage area (Plate 1). Lines were flown 200 m apart at an elevation of 30 m wherever permissible by FAA regulations (*Smith et al.*, 2003). Measurements of ambient electromagnetic noise, such as the disturbance from power lines, were made for the

purpose of removing the cultural noise from the data during processing.

The RESOLVE system was calibrated both before and after use at the Fugro offices in Toronto to ensure that the instrument functioned properly. To measure instrument response without the effect of the electromagnetic properties of the ground, the system was flown to an elevation exceeding its sensitivity at the ends of each survey line. Figure 5.2 shows a section of the geological map from Plate 1 with an overlay of the survey lines. In Figure 5.3, the geological map and 18 survey lines chosen for analysis in this presentation are used as an overlay on the Google Earth satellite image of the field area.

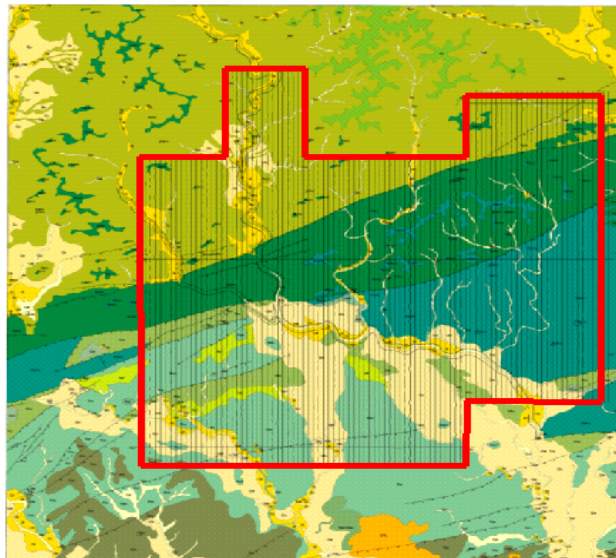


Figure 5.2: Map of the survey area as an overlay on geological map (*Smith et al. 2003*).

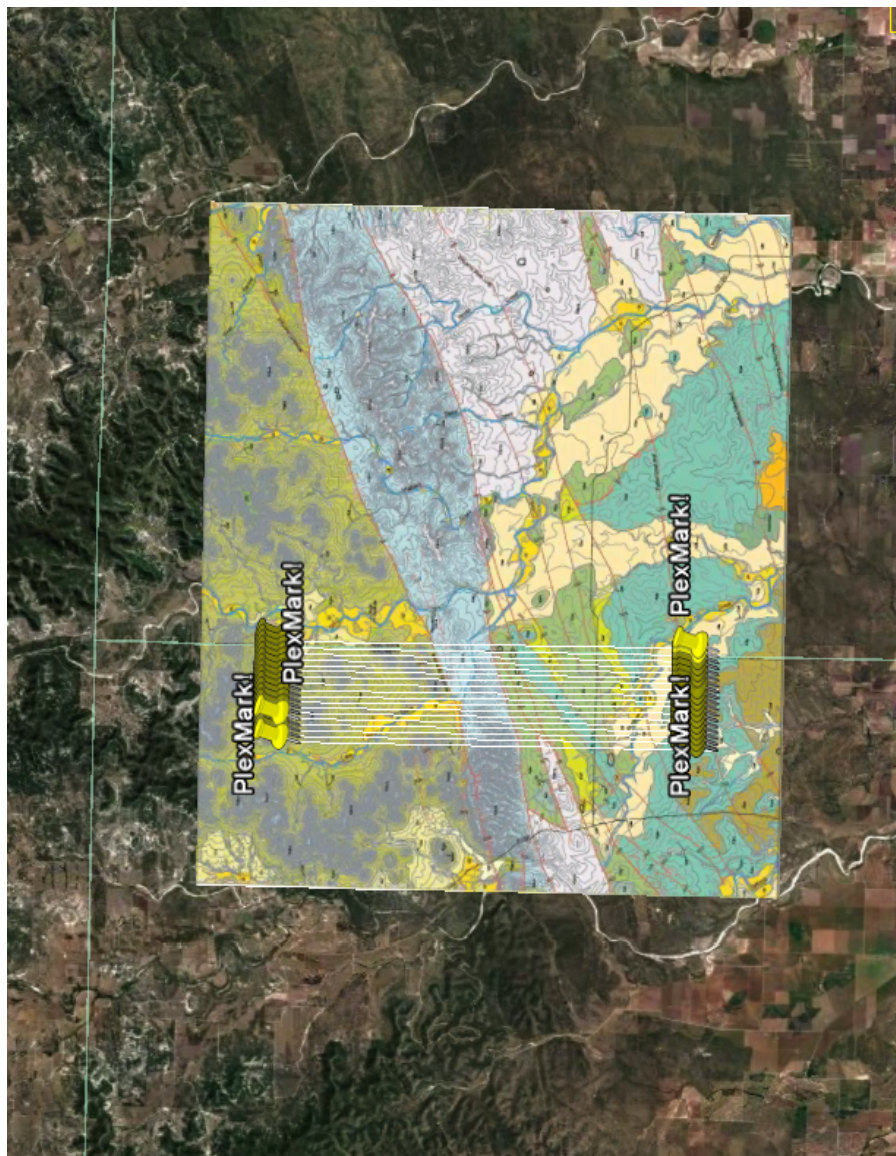


Figure 5.3: Geology map over Google Earth Satellite image of field site with survey lines analyzed marked in white.

VI. DATA ANALYSIS

6.1 Resistivity Maps

The report by Smith *et al.* (2003) gives apparent resistivity maps for each of the frequencies. The apparent resistivities as shown in the maps (Figure 6.1, a-e) are equal to the true resistivity if the earth were actually a homogeneous half-space. In reality, the different sedimentary rock units noted in Section II have slightly different compositions, particle sizes, porosities, and fracture densities, all of which determine the electrical conductivity. The term “apparent resistivity” describes the composite response given by electrical properties produced by horizontal and vertical inhomogeneities in the underlying strata (Fraser, 1978). The resistivities in Figure 6.1 may be correlated with the geology mapped in Plate 1. The intermediate resistivities in the northwest are attributed to the Glen Rose Formation, exposed on the up-dip side of the Woodard Cave fault (Smith *et al.*, 2003). Towards the center of each resistivity map, the resistive Devils River Formation is exposed. The difference in resistivity between the highest frequency (100 kHz) and the second highest (25 kHz) is due to a compositional difference between the Upper and Lower Devils River Formations. The section of high resistivity seen over Seco Creek in the northwestern part of the map is possibly due to the existence of more resistive limestone at depth (Smith *et al.*, 2003). The Del Rio Clay appears as areas of low resistivity. Features towards the center of the map correspond to known structure and stratigraphy and suggest additional structure that has not yet been mapped. For more detailed interpretation of the apparent resistivity maps, see Smith *et al.* (2003).

The level of water in the unconfined zone of the aquifer is monitored throughout the year by the Edwards Aquifer Authority at several test wells. The Edwards group appears at the surface in the recharge zone and plunges to the south until the top of the group reaches a depth of approximately 450 m below the surface (*Edwards Aquifer website*, 2007). Above the Edwards aquifer is the more conductive Del Rio Clay and younger limestone groups.

The presence of the conductive Del Rio Clay layer, which crops out in the southern portion of the map, suggests that even the 400 Hz frequency cannot penetrate the aquifer unit (Table 5.2). The effect of the saturated aquifer rocks influences the resistivity plots as the plots are of apparent resistivity, making it difficult to tell whether the resistivity survey is measuring the effect of the less resistive units or the presence of water.

Currently, no geological transects are available immediately over the survey area.

Interpolations for the survey area developed by using the available transects on either side of the survey area are subject to error due to the complexity of the fault system. A profile for the survey area will help to accurately determine the depth to aquifer units to resolve the question of the source of the high conductivity region.

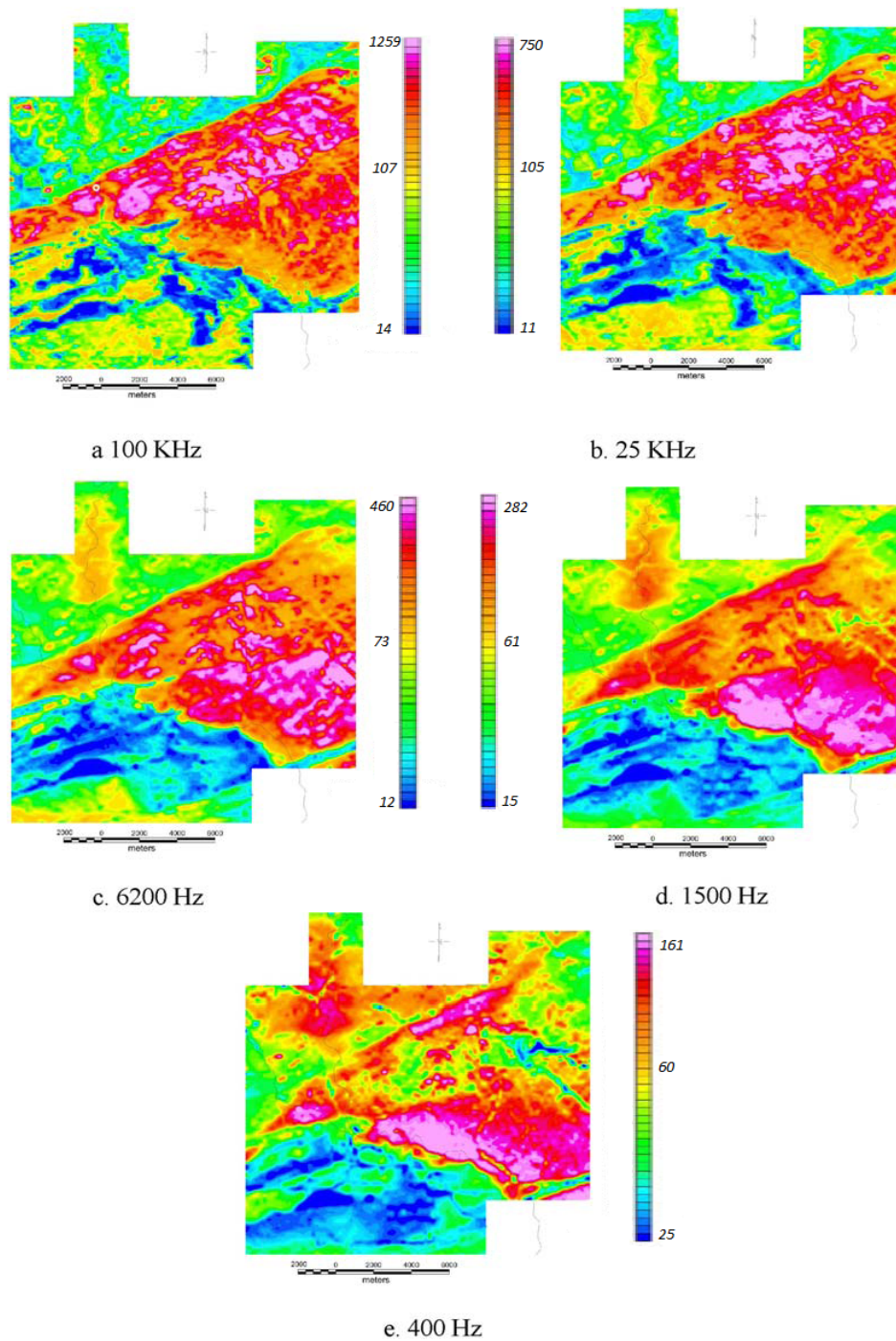


Figure 6.1: Maps of apparent resistivity for the horizontal coplanar coil pairs. High resistivities are warm colors with values given in ohm meters. The highest apparent resistivities appearing on each plot are a. 1300, b. 800, c. 500, d. 300, and e. 150 ohm meters (*Smith et al. 2003*).

The brief analysis by the USGS does not explicitly consider lateral roughness in terms of length-scale dependent fracture properties. This is a main contribution of this thesis.

Vertical roughness has already been described by the parameter β_v . To quantify lateral roughness along the survey lines, a second parameter, β_H , is introduced. The effort to detect lateral roughness is motivated by the suggestion of detailed subsurface structure that has yet to be mapped (*Smith et al.*, 2003). *Matlab* code was developed to process data from the twelve westernmost survey lines (Figure 5.3), flown over the catchment zone, recharge zone, and confined zone of the aquifer (Figure 2.2), as well as the Woodard Cave Fault. The latter marks the contact between the Glen Rose Limestone and the lower Devils River Formation (Plate 1).

A Fast Fourier Transform (FFT) was applied to each line of the HEM response data. The power spectral density (PSD) of apparent resistivity, ρ_a , dependent on spatial wavenumber f , was then plotted to observe the general trend of the curves for each frequency. A representative PSD plot is shown in Figure 6.2. Plots for the remaining five lines are given in the Appendix for comparison (Figure A-1). A 2002 study by Everett and Weiss indicates that the PSD plotted for a signal received from controlled-source electromagnetic experiments is an example of fractional Brownian motion instead of an example of a smooth, piecewise homogeneous signal with small-scale variations due to noise.

Using a power law of the form

$$|A(f)|^2 \sim f^{\beta_H} \quad (6.1),$$

the slope of the PSD is the value of β_H (Everett and Weiss 2002). Upon first observation, it is apparent that the general slope of all curves graphed is such that $|\beta_H| > 0$, as is the case when lateral heterogeneity exists.

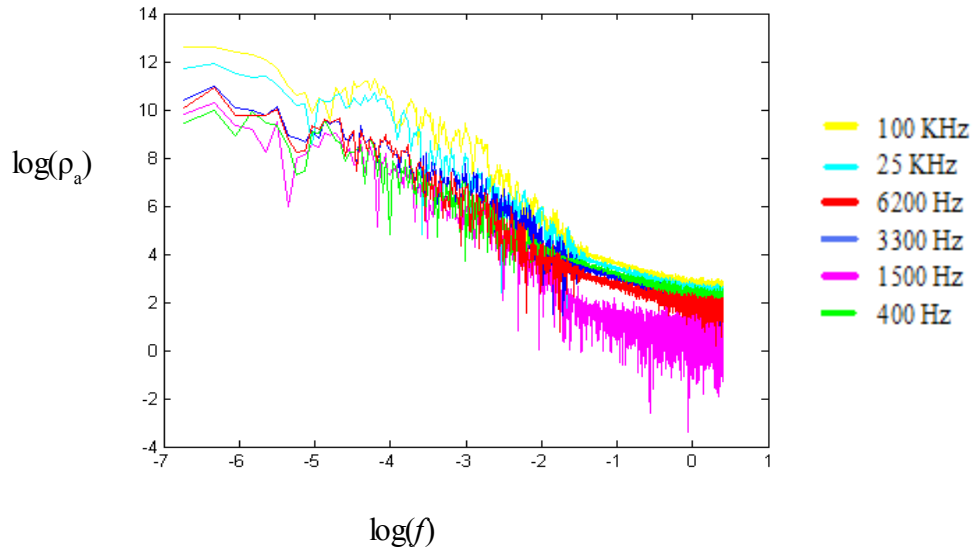


Figure 6.2: Plot of the PSD for Line 4. Slope of curves overall are <1 such that $|\beta_H| > 0$. As the value of β_H increases, signifying increased roughness, the slope of the PSD

increases (Everett and Weiss, 2002). The slope of the PSD overall appears to be <1 , but varies locally with wavenumber. For each coil frequency, the HEM apparent resistivity along the line is broken down into 256-point windows and least-squares regression was performed as the window is slid across the profile to plot the value of β_H v. position. In a 2003 study by Dhu *et al.*, the fractal dimension of Australian regolith was examined in a similar way. A least-squares fit line was used to calculate fractal dimension for the PSD plot of three frequencies using a sliding window of 33 points. In this study, a fractal signal appeared when the fractal dimension was >1 and it was found that this was the case for all but the latest time windows, where the signal trended toward Gaussian noise. The paper showed a connection between regions of high resistivity and low fractal dimension and supported the conclusion by Everett and Weiss (2002) that the EM response of the subsurface is from rough geology and not from smooth, continuous layers with Gaussian noise superimposed on the signal (Dhu *et al.*, 2003).

For the Edwards aquifer survey, survey points were collected with a spacing of 3 m such that position 1 correlates to 0 m from the origin of the survey line, position 2 correlates to 3 m from the origin of the survey line, position 3 correlates to 6 m from the origin of the survey line, and so on. Figure 6.3 shows an example of a β_H v. position plot. Plots for the remaining lines are found in the Appendix as Figures A-2. The plot shows the change in fractal dimension (β_H) along the length of the survey line for each of the six frequencies. The frequencies correspond to different depths of penetration and differences in β_H for different frequencies are indicative of variation in structure with depth. For all six

frequencies, the value of β_H is > 0 near the beginning of the flight lines and trends towards Gaussian noise at the end of the lines.

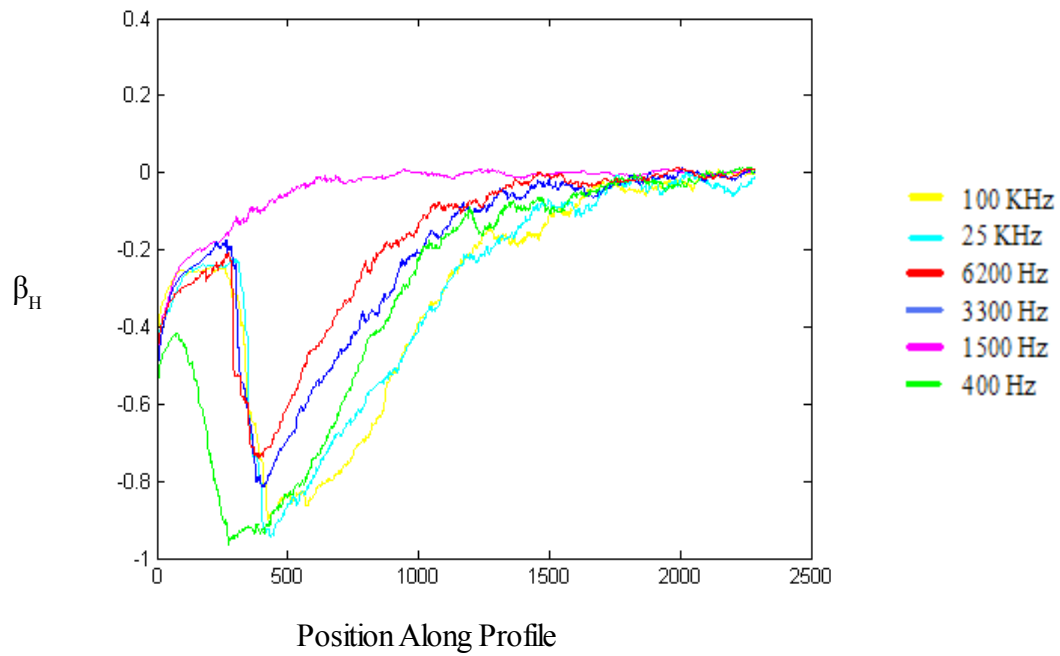


Figure 6.3: Plot of β_H v. position along Line 4. Note that towards the end of the profile, $\beta_H \rightarrow 0$, the value at which the response becomes pure Gaussian noise.

6.2 β_H Maps

The data for 18 of the HEM survey lines from Seco Creek, pictured in Figure 5.3, were processed using the methods described in Section 6.1.1. The data from the plots of β_H v. position along a survey line were combined and plotted with interpolated contours to make a map of apparent β_H for the area covered by the lines. Map view plots of the β_H values for the various frequencies are pictured in Figure 6.4.

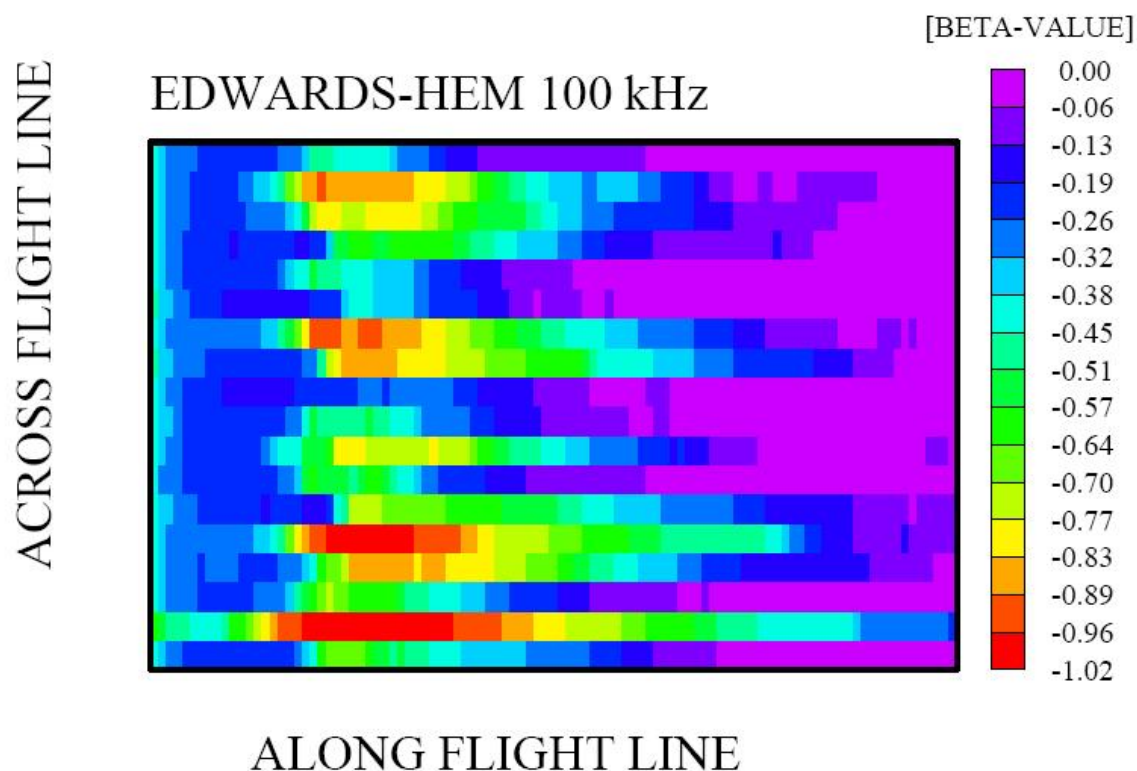


Figure 6.4: Maps of β_H (not to scale) for 18 processed survey lines from the plots of β_H v. position along line (as shown in Figure 6.3 and Appendix, Figure A-2). Flight line number is on y-axis with line 1 in the lower left corner and line 18 in the upper right corner. Distance along the flight lines is expressed from distance = 0 km to 50 km.

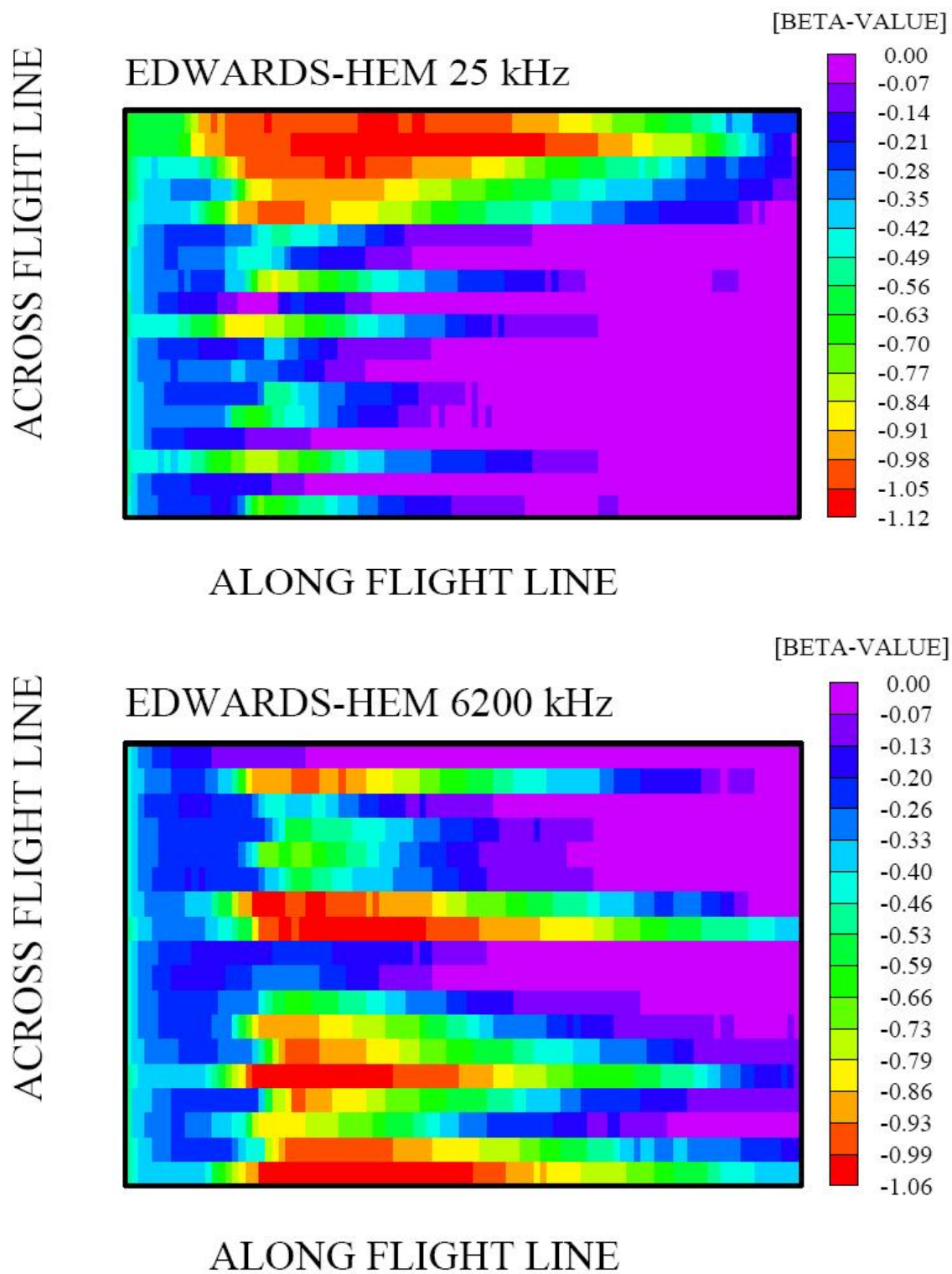


Figure 6.4, continued

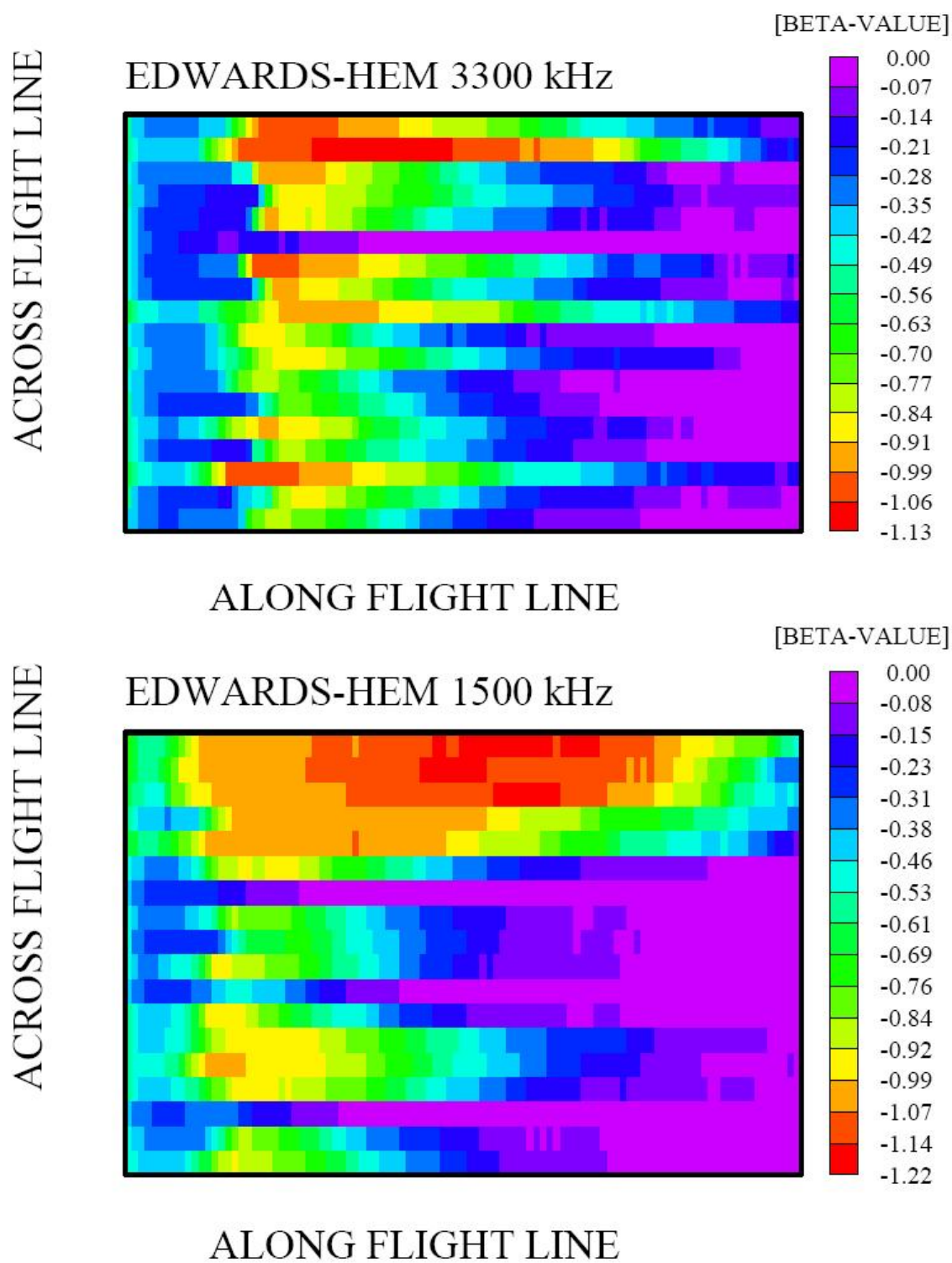


Figure 6.4, continued

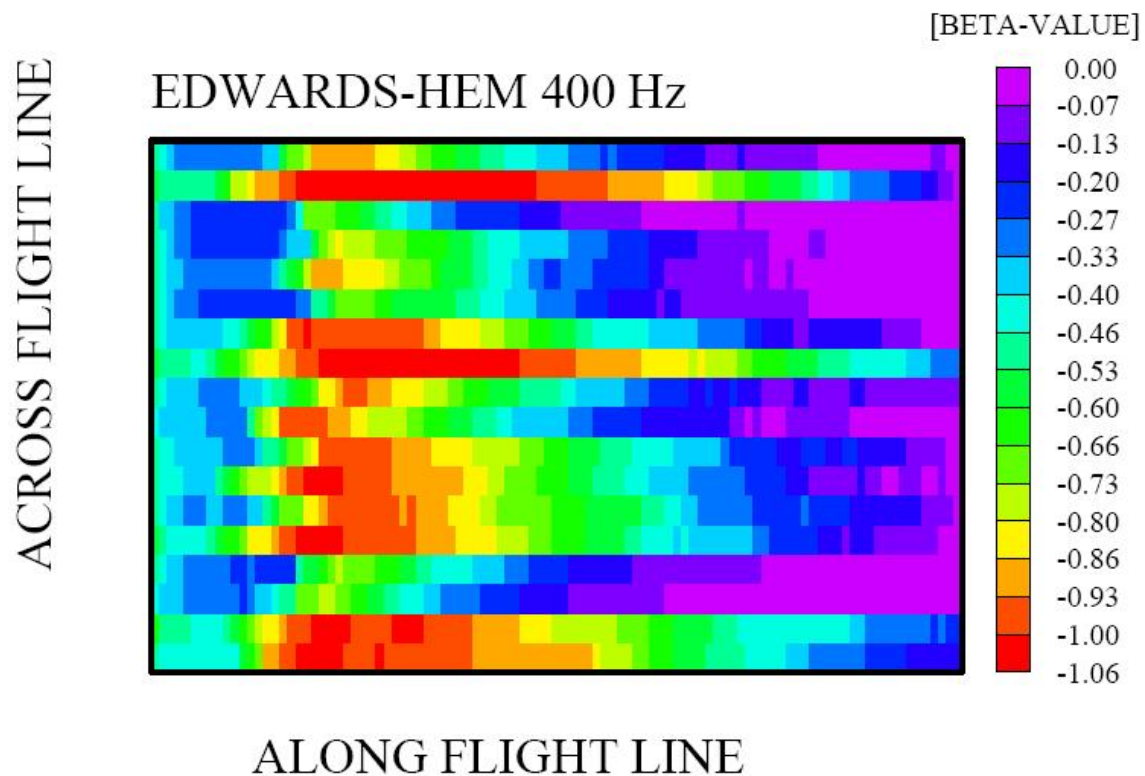


Figure 6.4, continued

To relate the β_H maps to the geology in the Edwards aquifer, overlays of the β_H contour plots in Figure 6.4 were added one at a time to the basic geological map shown in Figure 5.3. Overlays are transparent enough so that the geological faults and contacts are visible beneath the contour plots. An example of the map for 100 kHz is provided in Figure 6.5.

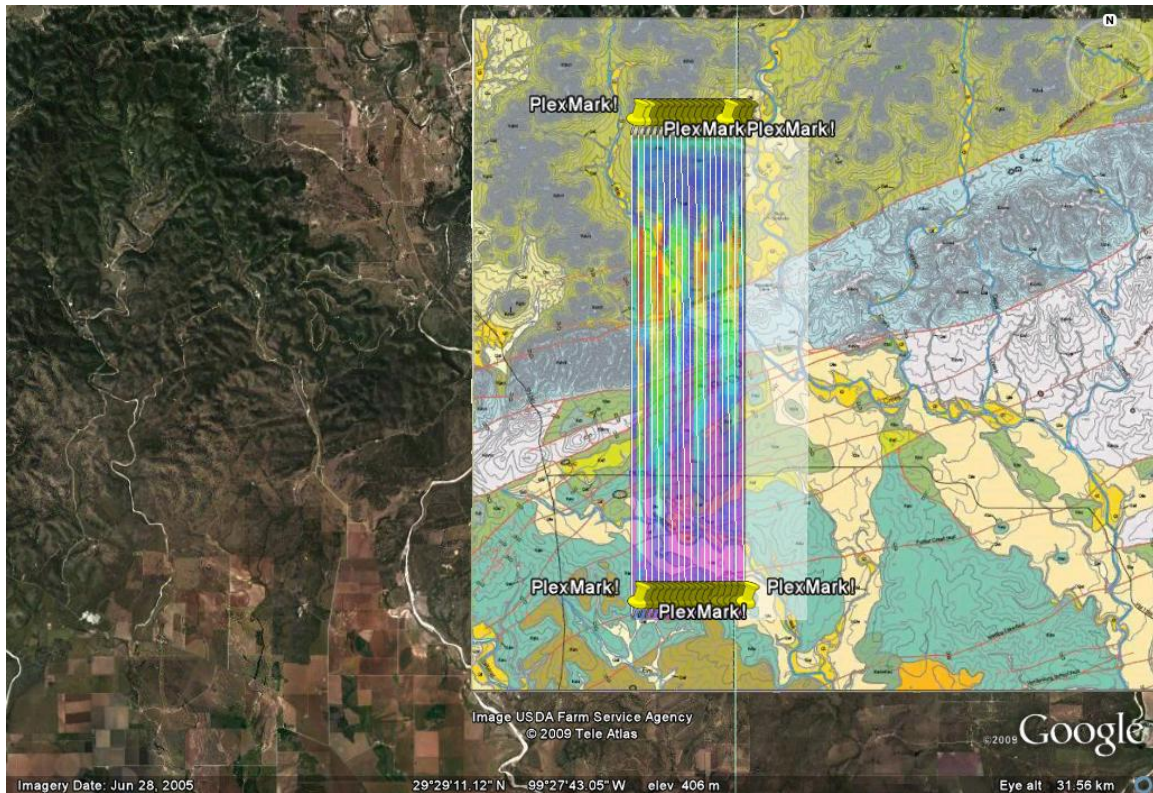


Figure 6.5: The β_H map for 100 kHz is aligned with the survey lines. It is set as a transparency to determine whether values of β_H such that $0 < |\beta_H| < 1$ are related to stratigraphic or structural features.

The region of highest β_H values is located over the Woodard Cave Fault, which is the contact between the Glen Rose Limestone to the north (up-dip) and the lower Devils River Formation to the south (down-dip). The Hill Country State Natural Area has a recorded elevation change over the Woodard Cave Fault of at least 60 m. Remnants of the lower Devils River Formation lie on top of the Glen Rose Limestone in the north, indicating some large-scale erosion of the lower Devils River Formation after movement

occurred along the fault. Several other fault traces are found on the up-dip side of the fault line and more are marked south of the unnamed fault that occurs as the contact between the lower Devils River Formation and the Buda Limestone. The frequency is an indication of relative depth of penetration, in accordance with the electromagnetic skin effect (Table 5.2). In an effort to determine whether the structure causing the large β_H values is pervasive throughout the full range of depth for the RESOLVE system, the plot of the β_H map for the lowest frequency, 400 Hz, is provided in Figure 6.6. Overlays of the β_H maps for the remaining four frequencies were also created. Maps of each individual frequency plotted as overlays are shown in Figures A-3 in the Appendix.

High β_H values for the low-frequency case (400 Hz) are seen in approximately the same area as the high values in the plot for the high-frequency case (100 kHz). The heterogeneity appears to be present beyond the depth of the survey. A plot of β_H maps for all six frequencies is given in Figure 6.7 in order to see whether the responses from all frequencies display high β_H values in similar areas. The high values of β_H from each individual frequency are mostly concentrated at and to the north of the Woodard Cave Fault.

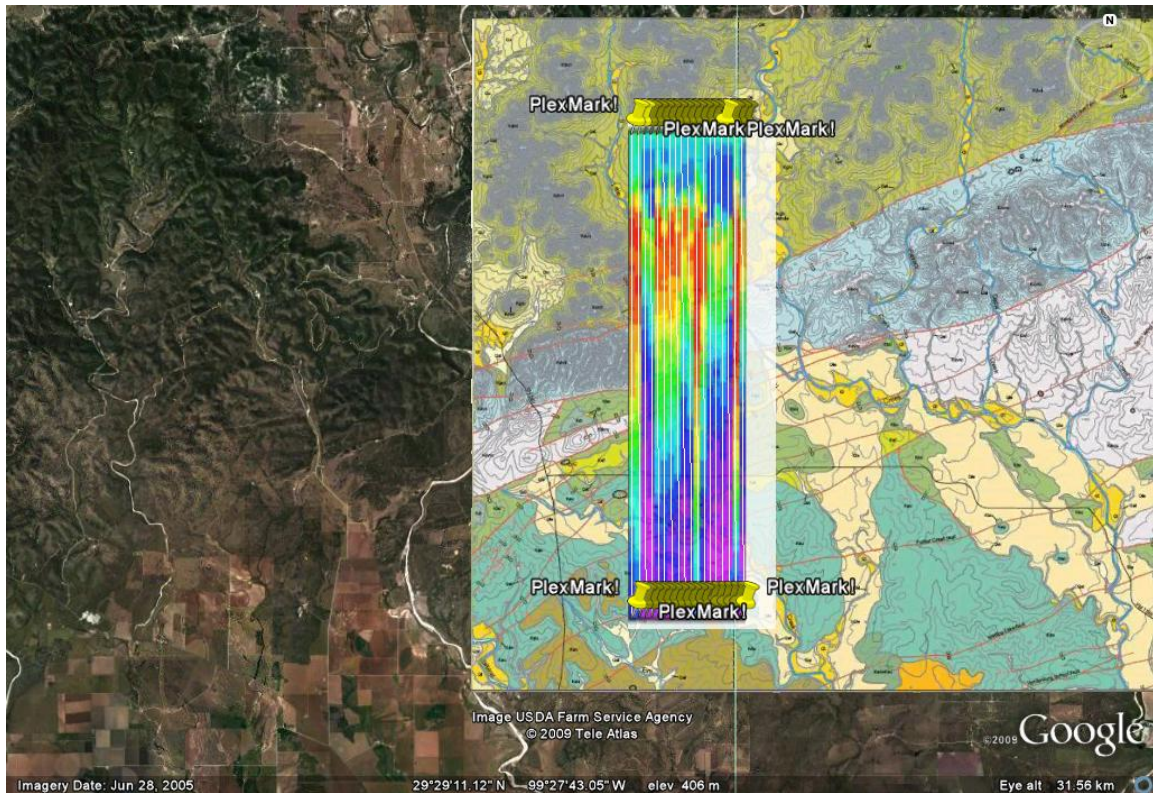


Figure 6.6: Overlay of β_H map for 400 Hz.

The existence of high β_H values for all frequencies near the Woodard Cave Fault suggests that roughness exists at all depths to which the frequencies used in the survey can probe. Large faults produce smaller associated faults (*Childs et al.*, 1995), resulting in higher values of β_H on and around the Woodard Cave Fault. The distribution of the higher β_H values is asymmetrical about the fault. This is likely a result of differences in mechanical strength between the Glen Rose Limestone to the north, which is more contiguous, and the Devils River Formation to the south, which is known to have extensively connected

pore spaces due to dissolution, as discussed in Section II. The asymmetric distribution of β_H may also result from the fault trace descending at an angle such that the fault trends to the north. A geological profile will help to determine the cause of the asymmetry.

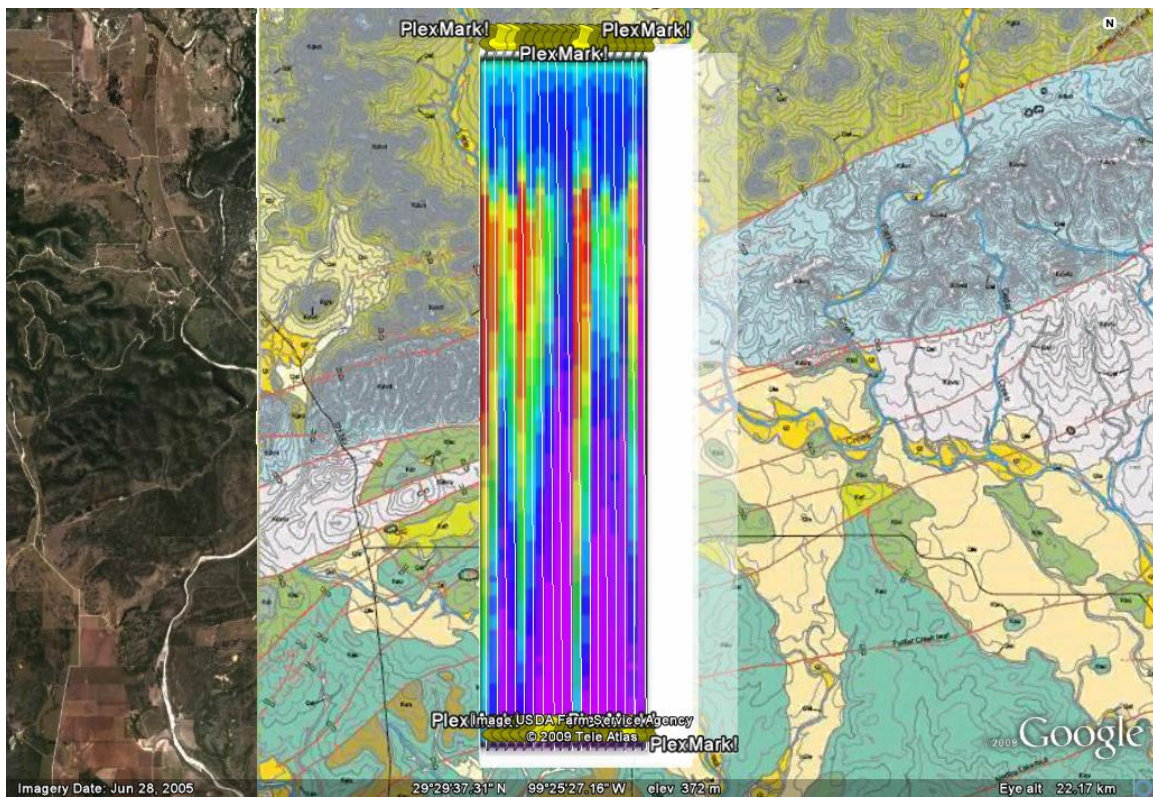


Figure 6.7: Overlay of β_H maps for all six frequencies.

VII. CONCLUSIONS AND RECOMMENDATIONS FOR FUTHER WORK

7.1 Conclusions

The appropriateness of the “rough” model for geological media has been investigated in the study presented here. According to the new theory of rough CSEM responses, synthetic models that contain rough layers characterized by non-zero values of β_V show that CSEM depth soundings deviate significantly from the classical electromagnetic response when all layers are smooth and homogeneous. Lateral models of heterogeneity, cast in terms of a second roughness parameter β_H , were also produced to show rough structure indicative of the subsurface fracture distribution. The PSD apparent resistivity plot in Figure 6.2 and the additional plots in Appendix Figures A-1 show an increase in slope near the region of most extensive faulting. A power law PSD cannot be generated with a continuous (smooth) conductivity layer model with lateral variation (*Everett and Weiss, 2002*).

The extensive fracturing of the Edwards aquifer and surrounding sedimentary rock units is well-documented. The fracturing likely generates both conduits and blockages to water flow in the aquifer, but much of the structure lies below the surface and has yet to be discovered. In the 2003 USGS study of the Seco Creek Area (*Smith et al.*), the HEM airborne electromagnetic survey detected all known faults and may have also detected previously unknown buried structures. Processing the six-frequency data collected using

the RESOLVE 6 system enables one to look at the lateral heterogeneity of the area at six different skin depths by mapping the β_H parameter. β_H is obtained by calculating the slope of the amplitude spectra of apparent resistivity using a best fit line for a sliding window of 256 points for each survey line and maps of β_H are constructed by interpolating the values of β_H along each survey line. An overlay of the β_H maps onto the geological map of the area allows for a first pass at interpreting the effect of structure on β_H . High values of β_H are seen over the Woodard Cave Fault with β_H decreasing with distance away from the fault trace. Since the value of β_H is determined by the scale of fracturing, it is safe to assume that the high values are related to the existence of the fault itself and the associated pervasive, large-scale fracturing nearby. The magnitude of β_H decreases as fracture density and connectivity in the damage zone diminishes.

Given this interpretation, the slow decrease in β_H with distance to the north compared to the much more rapid decrease in β_H to the south of the fault may suggest some difference in the mechanical strength between the Glen Rose Limestone and the lower Devils River Formation, likely due to the more contiguous nature of the Glen Rose Limestone.

Another possibility is that the Woodard Cave Fault's fault trace descends at an angle instead of vertically downward so that the associated fracturing appears from the surface to be concentrated to the north.

7.2 Recommendations for Further Work

A primary recommendation is to test the synthetic 1-D soundings presented in Section IV with field experiments and then to further develop the connection between β_V and β_H . An understanding of the relationship between vertical and lateral heterogeneity would greatly enhance our ability to interpret the depth extent of heterogeneity and model any anisotropy in roughness parameters β_V and β_H for field experiments. To further explore the connection between , it would be useful to develop forward modeling of the CSEM response for a rough 2-D conductivity model. The governing equation is the fractional-order generalization of the pre-Maxwell diffusion equation (*Weiss and Everett, 2007*).

The interpretation of the relationship between geological structure and β_H given above is a first approximation of a complete geological interpretation of the HEM data. It can be said, however, that the β_H maps present an interesting complement to the apparent resistivity maps and give valuable information about structure that cannot be obtained by other geophysical methods. To draw definite conclusions, a team of expert geophysicists, hydrologists and structural geologists should work together to build the best possible hydrogeological description of the important Edwards aquifer.

REFERENCES

- Abbott, P.L., 1975, On the hydrology of the Edwards limestone, south-central Texas, *Journal of Hydrology*, **24**, 251-269.
- Barker, R.A., and A.F. Ardis, 1996, Hydrogeologic framework of the Edwards-Trinity aquifer system, west-central Texas, U.S. Geological Survey, Professional Paper 1421-B, 61 p.
- Berkowitz, B., 2002, Characterizing flow and transport in fractured geological media: A review, *Advances in Water Resources*, **25**, 861-884.
- Blome, C.D., J.R. Faith, E.W. Collins, D.E. Pedraza, and K.E. Murray, 1994, Geologic Map Compilation of the Upper Seco Creek Area, Medina and Uvalde Counties, south-central Texas, U.S. Geological Survey Open File Report 2004-1430, 21 p.
- Bonnet, E., O. Bour, N.E. Olding, P. Davy, I. Main, and B. Berkowitz, 2001, Scaling of fracture systems in geological media, *Reviews of Geophysics*, **39**, 347-383.
- Bour, O., and P. Davy, 1997, Connectivity of random fault networks following a power law fault length distribution, *Water Resources Research*, **33**, 1567-1583.
- Cain, M.J., 2002, Logistics Report, Helicopter-borne RESOLVE electromagnetic and magnetic geophysical survey, Seco Creek, Texas, Fugro Airborne Surveys, Report #6025.
- Chave, A.D., 1983, Numerical integration of related Hankel transforms by quadrature and continued fraction expansion, *Geophysics*, **48**, 1671-1686.
- Childs, C., J. Watterson, and J.J. Walsh, 1995, A model for the structure and development of fault zones, *Journal of the Geological Society*, **56**, 183-192.
- Choquette, P.W., and L.C. Pray, 1970, Geologic nomenclature and classification of porosity in sedimentary carbonates, *AAPG Bulletin*, **54**, 207-250.
- Cladouhos, T.T., and R. Marrett, 1996, Are fault growth and linkage models consistent with power-law distributions of fault lengths?, *Journal of Structural Geology*, **18**, 281-293.
- Collins, E.W., 1987, Characterization of fractures in limestones, northern segment of the Edwards aquifer and Balcones fault zone, central Texas, *Gulf Coast Association of Geological Societies Transactions*, **37**, 43-54.

Collins, E.W., 1995, Structural framework of the Edwards aquifer, Balcones fault zone, central Texas, Gulf Coast Association of Geological Societies Transactions, **XLV**, 135-142.

Collins, E.W., and S.D. Hovorka, 1997, Structure map of the San Antonio segment of the Edwards aquifer and Balcones fault zone, south-central Texas: Structural framework of a major limestone aquifer: Kinney, Uvalde, Medina, Bexar, Comal, and Hays Counties: The University of Texas at Austin, Bureau of Economic Geology Miscellaneous Map No. 38, scale 1:250,000, 14 p. text.

Cook, P.G., and S. Kilty, 1992, A helicopter-borne electromagnetic survey to delineate groundwater recharge rates, Water Resources Research, **28**, 2953-2961, 1992.

Deike, R.G., 1991, Comparative petrology of cores from two test wells in the eastern part of the Edwards aquifer, south-central Texas, U.S. Geological Survey Water-Resources Investigations, Report 87-4266, 135 p..

Dhu, T., G. Heinson, and J. Joseph, 2003, The Hydraulic and Electrical Fractal Dimension of Regolith, *in* Roach, I.C., ed., Advances in Regolith, pp. 95-99, 2003.

Eckhardt, G., The Edwards Aquifer Website, Accessed 12-01-08
<<http://www.edwardsaquifer.net/>>.

Everett, M.E., 2009, Transient electromagnetic response of a loop source over a rough geological medium, Geophys. J. Int, **177**, 421-428, 2009.

Everett, M.E., and C.J. Weiss, 2002, Geological noise in near-surface electromagnetic induction data, Geophysical Research Letters, **29**, 10-1 – 10-4, 2002.

Ferrill, D.A., D.W. Sims, D.J. Waiting, A.P. Morris, N.M. Franklin, and A.L. Schultz, 2004, Structural framework of the Edwards aquifer recharge zone in south-central Texas, Geological Society of America Bulletin, **116**, 407-418.

Finn, C.A., T.W. Sisson, and M. Deszcz-Pan, 2001, Aerogeophysical measurements of collapse-prone hydrothermally altered zones at Mount Rainer volcano, Nature, **409**, 600-601.

Fraser, D.C., 1978, Resistivity mapping with an airborne multicoil electromagnetic system, Geophysics, **43**, 144-172.

Fugro Airborne, Fugro Airborne Surveys, Accessed 5-27-09
<<http://www.fugroairborne.com/>>.

Geonics Limited., TEM 47 Transmitter, Accessed 2-21-09
<<http://www.geonics.com/html/tem47.html>>

Gueguen, Y., C. David, P. Gavrilenco, 1991, Percolation and fluid transport in the crust. *Geophys. Res. Lett.*, **18**, 931-934.

Hovorka, S.D., A.R. Dutton, S.C. Ruppel, and J. Yeh, 1994, Sedimentologic and diagenetic controls on aquifer properties, Lower Cretaceous Edwards carbonate aquifer, Texas: Implications for aquifer management, *Transactions of the Gulf Coast Association of Geological Societies*, **XLIV**, 277-284.

Lucia, F.J., 1995, Rock-fabric/petrophysical classification of carbonate pore spaces for reservoir characterization, *AAPG Bulletin*, **79**, 1275-1300.

Maclay, R.W., and T.A. Small, 1986, Carbonate geology and hydrology of the Edwards aquifer in the San Antonio area, Texas: Texas Water Development Board, Report 296, 90 p.

Mandelbrot, B.B., D.E. Passoja, and A.J. Paullay, 1984, Fractal character of fracture surface of metals, *Nature*, **308**, 721-722.

Multala, J., H. Hautaniemi, M. Oksama, M. Lepparanta, J. Haapala, A. Herlevi, K. Riska, and M. Lensu, 1996, An airborne electromagnetic system on a fixed wing aircraft for sea ice thickness mapping, *Cold Regions Science and Technology*, **24**, 355-373.

Pantea, M.P., and J.C. Cole, 2004, Three-dimensional geologic framework modeling of faulted hydrostratigraphic units within the Edwards aquifer, northern Bexar County, Texas, U.S. Geological Survey, Scientific Investigations Report 2004-5226, 10 p.

Poon, C.Y., R.S. Sayles, and T.A. Jones, 1992, Surface measurement and fractal characterization of naturally fractured rocks, *J. Phys. D: Appl. Phys.*, **25**, 1269-1275.

Rose, P.R., 1972, Edwards group, surface and subsurface, central Texas: Austin, Bureau of Economic geology Report of Investigations, **74**, 198 p.

Ryu, J., H.F. Morrison, and S.H. Ward, 1970, Electromagnetic fields about a loop source of current, *Geophysics*, **35**, 862-896.

Schultz, R.A., C.H. Okubo, and S.J. Wilkins, 2006, Displacement-length scaling relations for faults on the terrestrial planets, *Journal of Structural Geology*, **28**, 2182-2193.

Singurindy, O., and B. Berkowitz, 2003, Evolution of hydraulic conductivity by precipitation and dissolution in carbonate rock, *Water Resources Research*, **39**, 1016; doi: 10.1029/2001WR001055, 2003.

Small, T.A., 1986, Hydrogeologic sections of the Edwards aquifer and its confining units in the San Antonio area, Texas, U.S. Geological Survey Water-Resources Investigations, Report 85-4259, 52 p.

Small, T.A., and A.K. Clark, 2000, Geologic framework and hydrogeologic characteristics of the Edwards aquifer outcrop, Medina County, Texas, U.S. Geological Survey Water-Resources Investigations, Report 00-4195, 10 p.

Smith, B.D., D.V. Smith, P.L. Hill, and V.F. Labson, 2003, Helicopter electromagnetic and magnetic survey data and maps, Seco Creek area, Medina and Uvalde Counties, Texas, U.S. Geological Survey, Open-File Report 03-226, 11 p.

"U.S. Census Bureau News". U.S. Census Bureau. 2-24-09
<<http://www.census.gov/Press-Release/www/releases/archives/population/013960.html>>

"U.S. Census Bureau, State and County Quickfacts". U.S. Census Bureau. 2-24-09
<<http://quickfacts.census.gov/qfd/states/48/4865000.html>>.

Weiss, C.J., and M.E. Everett, 2007, Anomalous diffusion of electromagnetic eddy currents in geological formations, *Journal of Geophysical Research*, **112**, B08102, doi:10.1029/2006JB004475.

APPENDIX

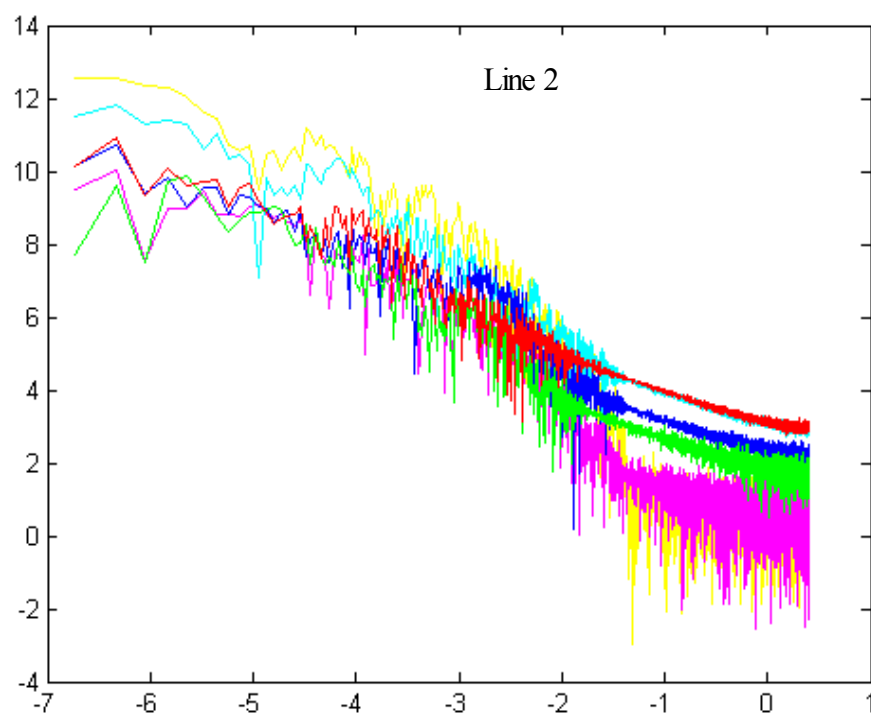
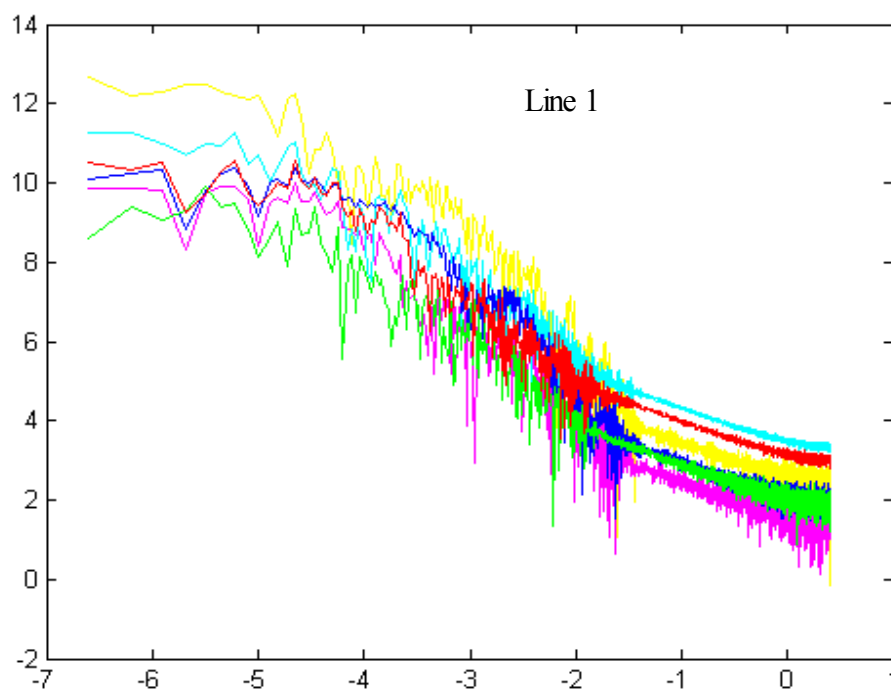


Figure A-1: Power spectral densities for lines 1, 2, 3, 5, and 6.

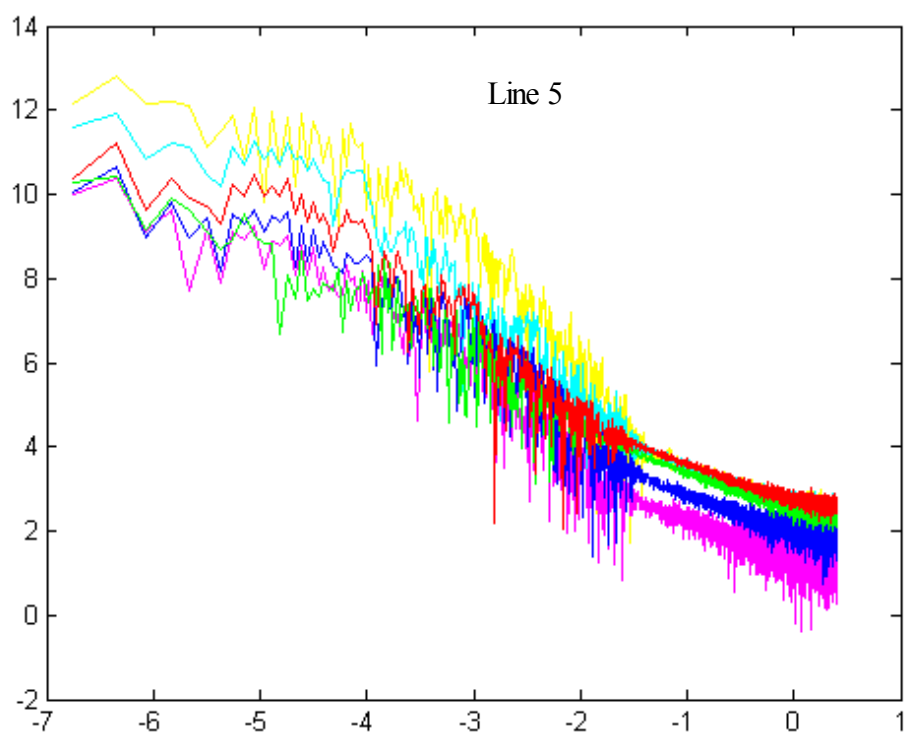
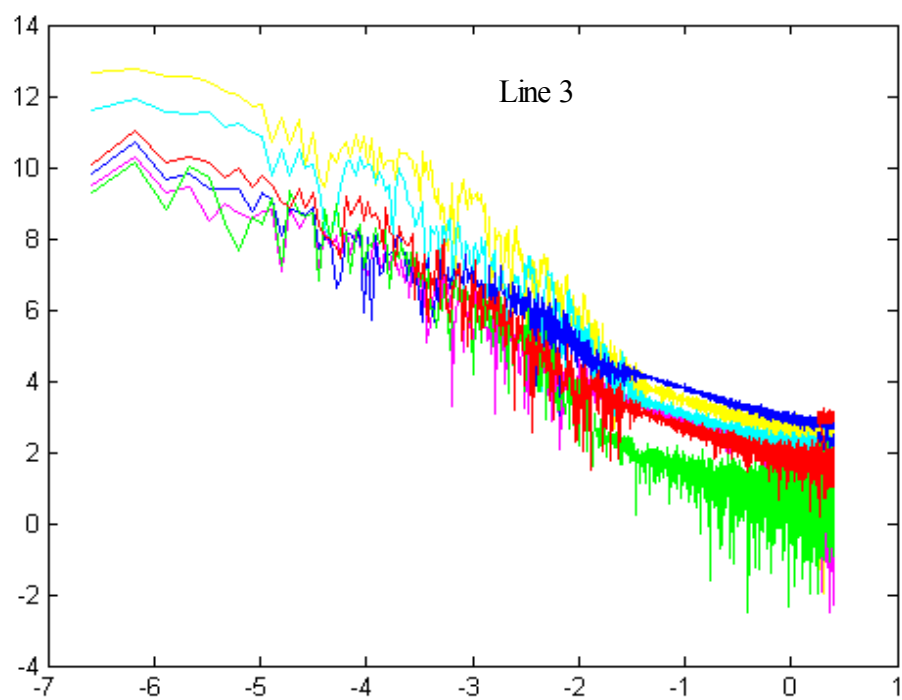


Figure A-1, continued

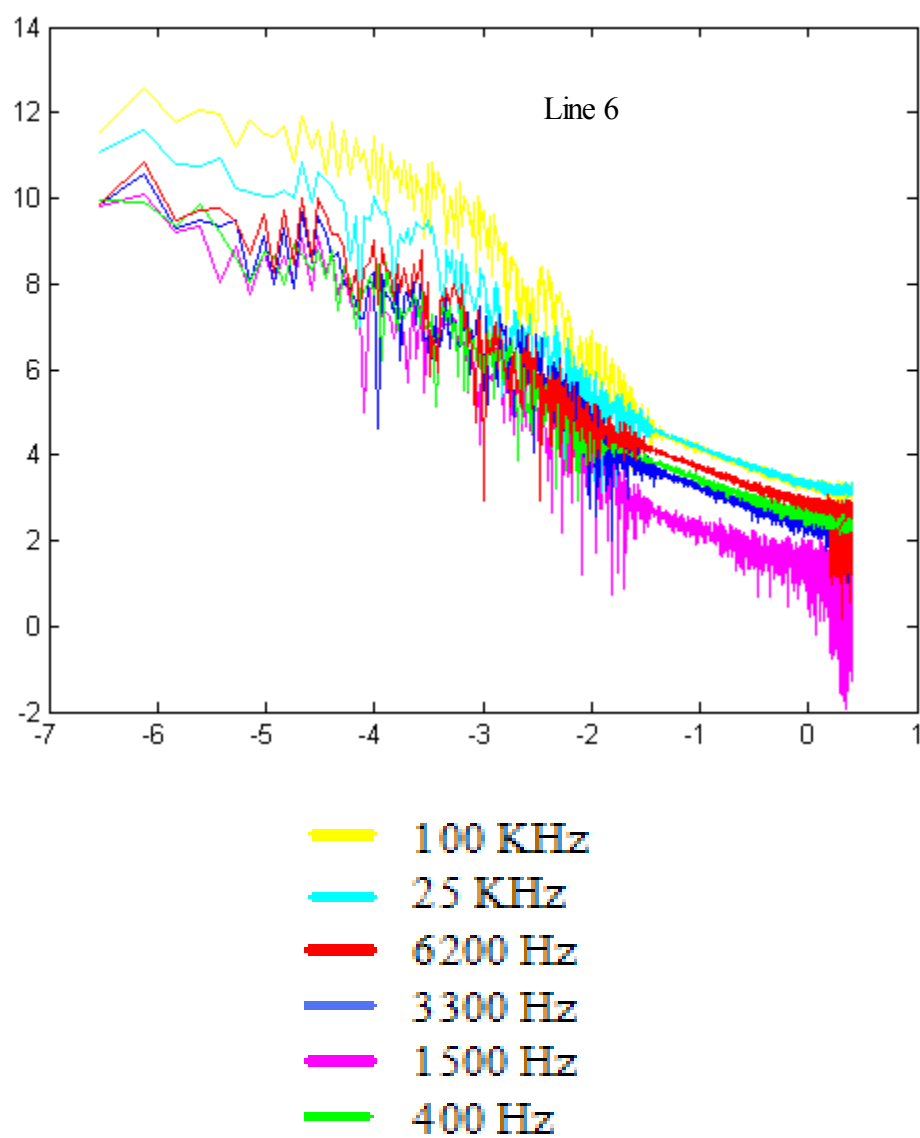


Figure A-1, continued

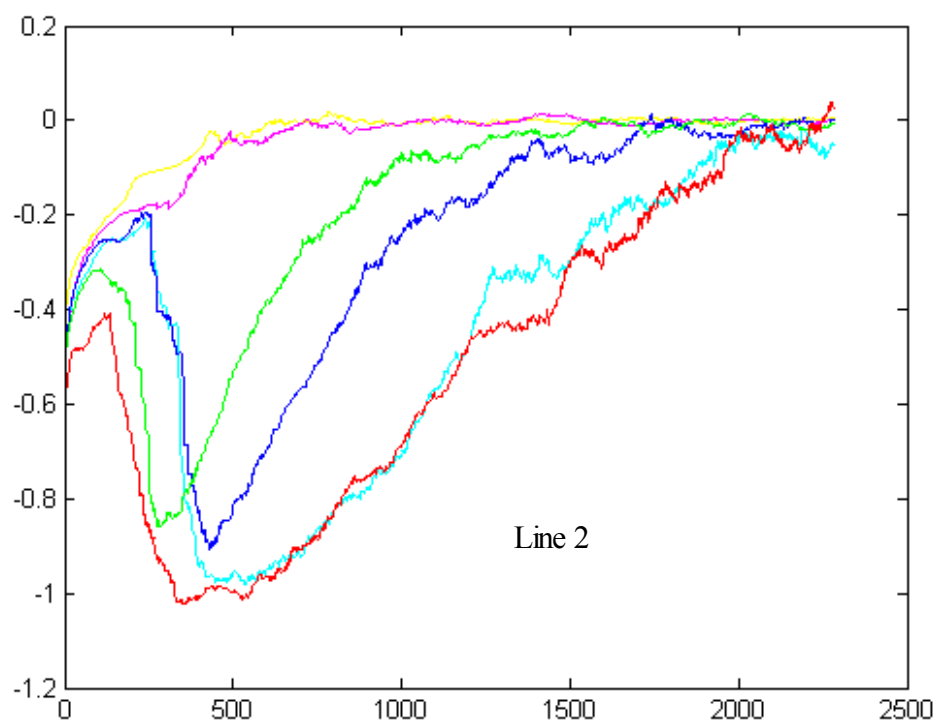
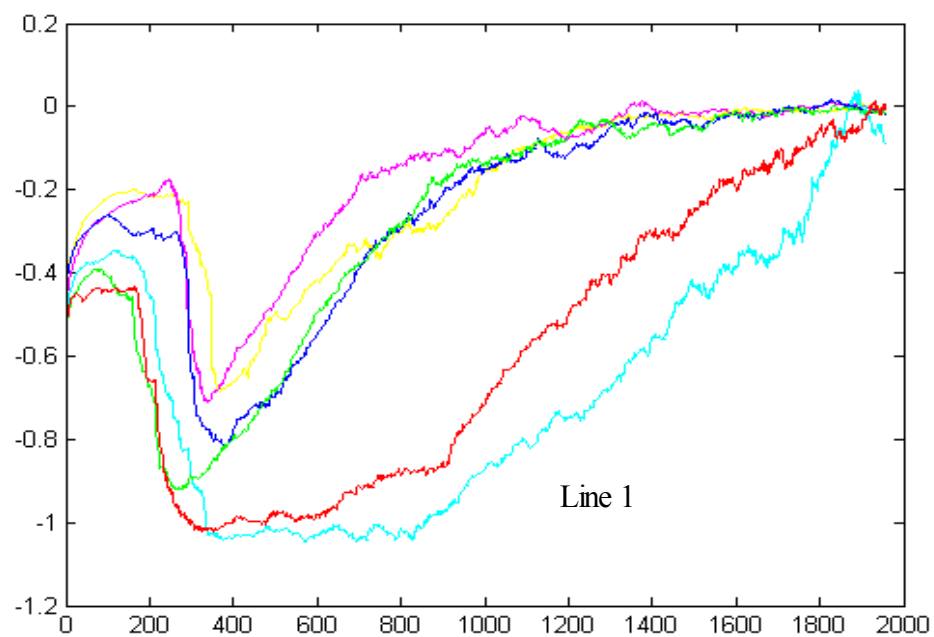


Figure A-2: Change in β_H with change in distance along survey line.

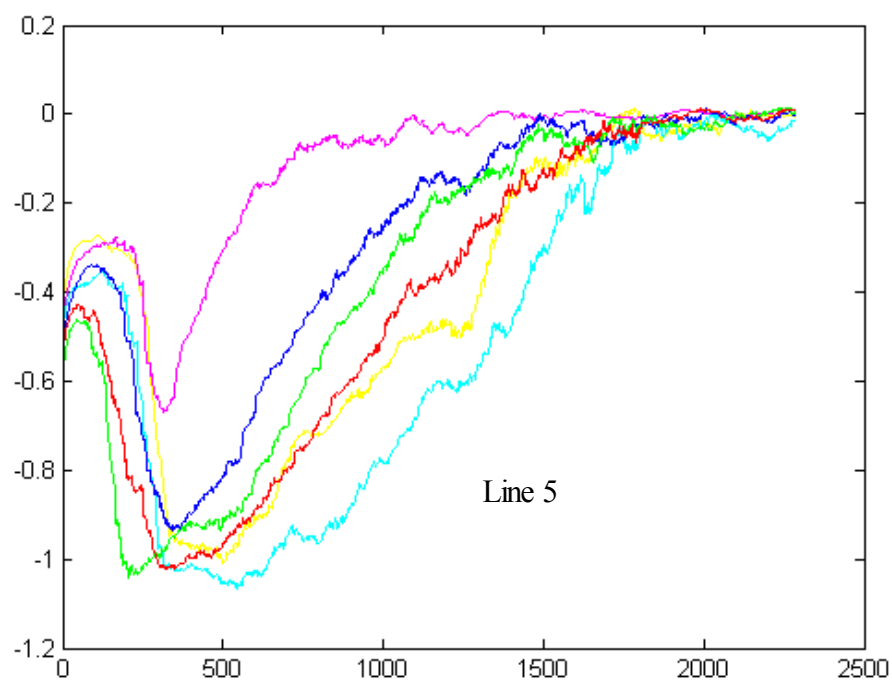
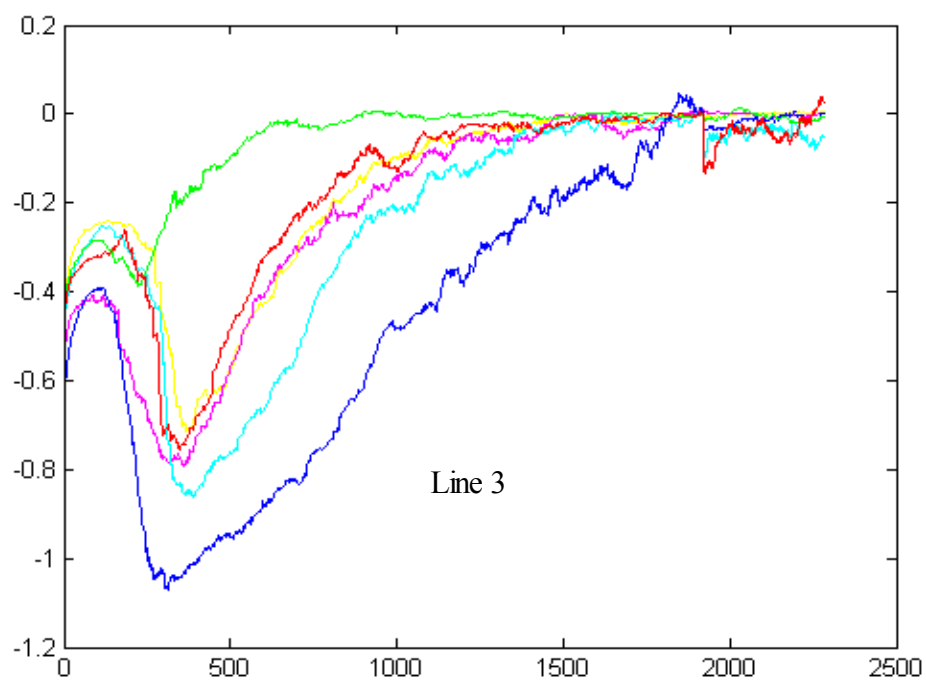


Figure A-2, continued

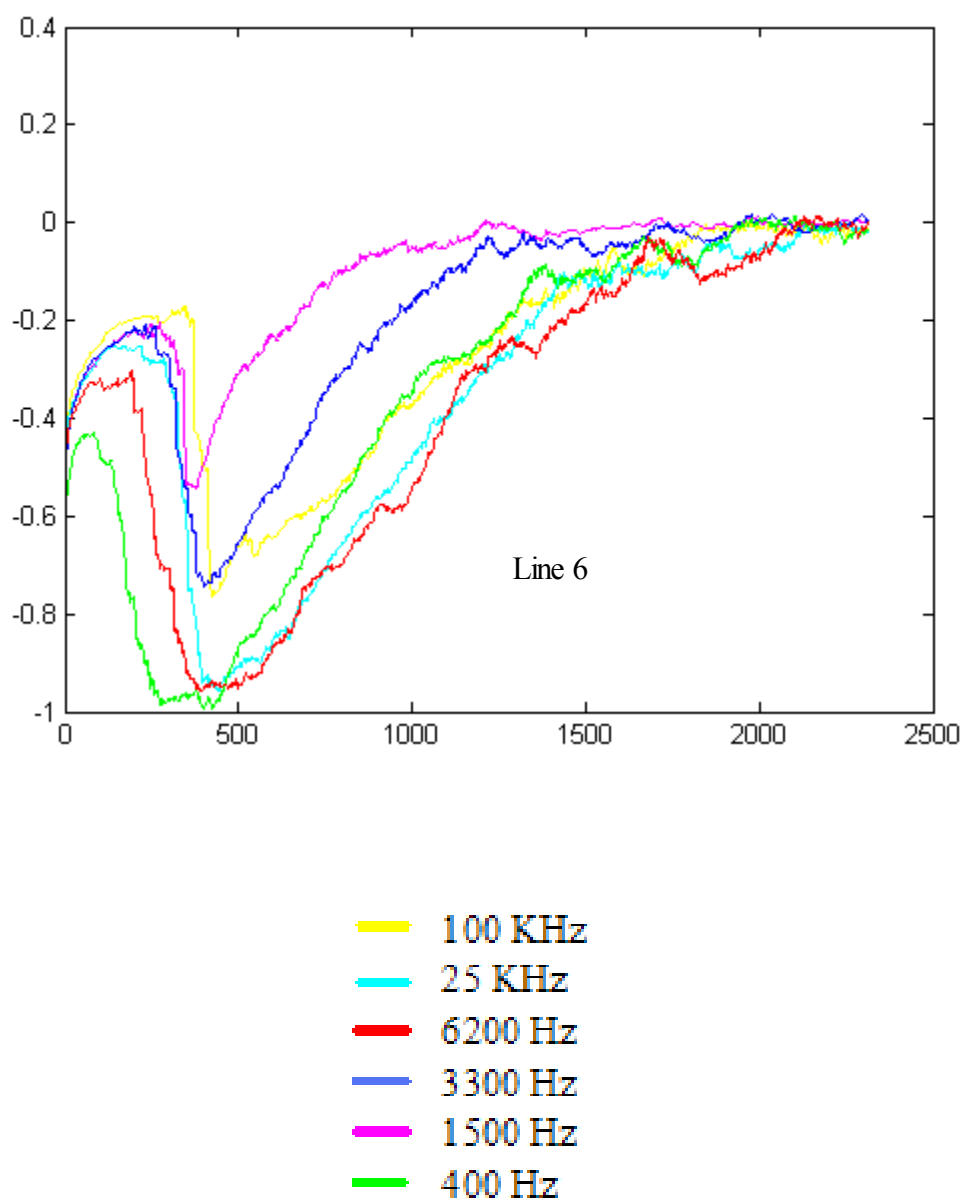
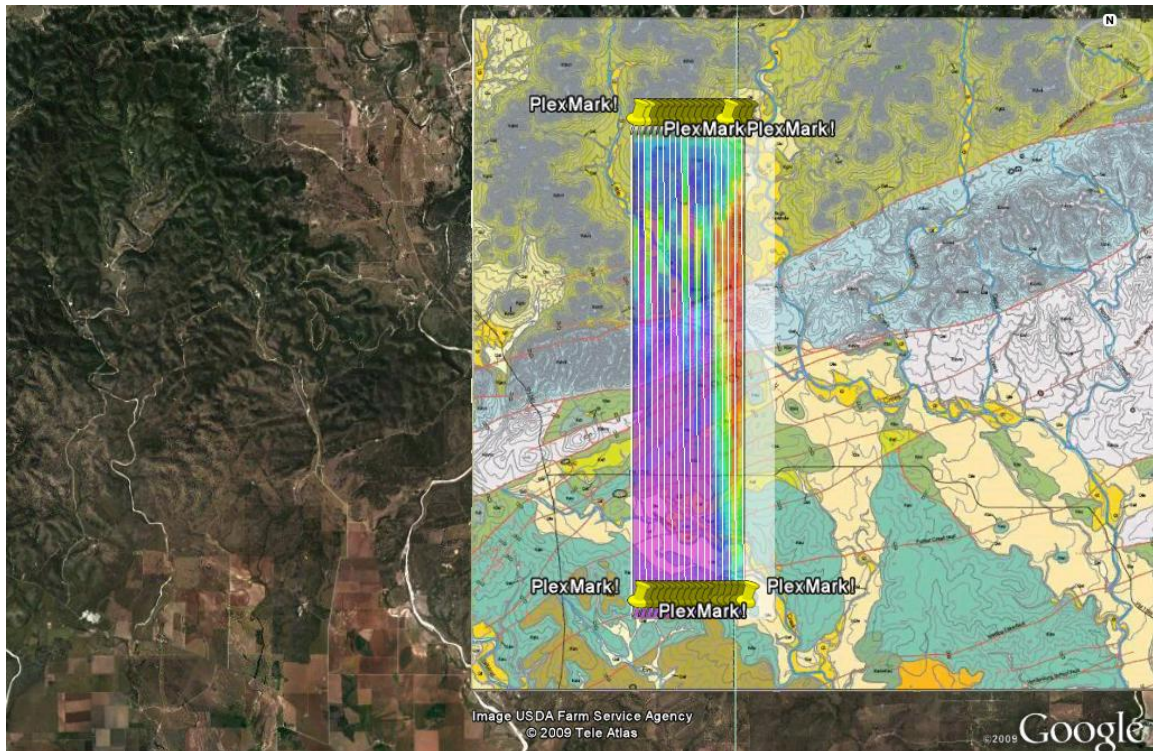
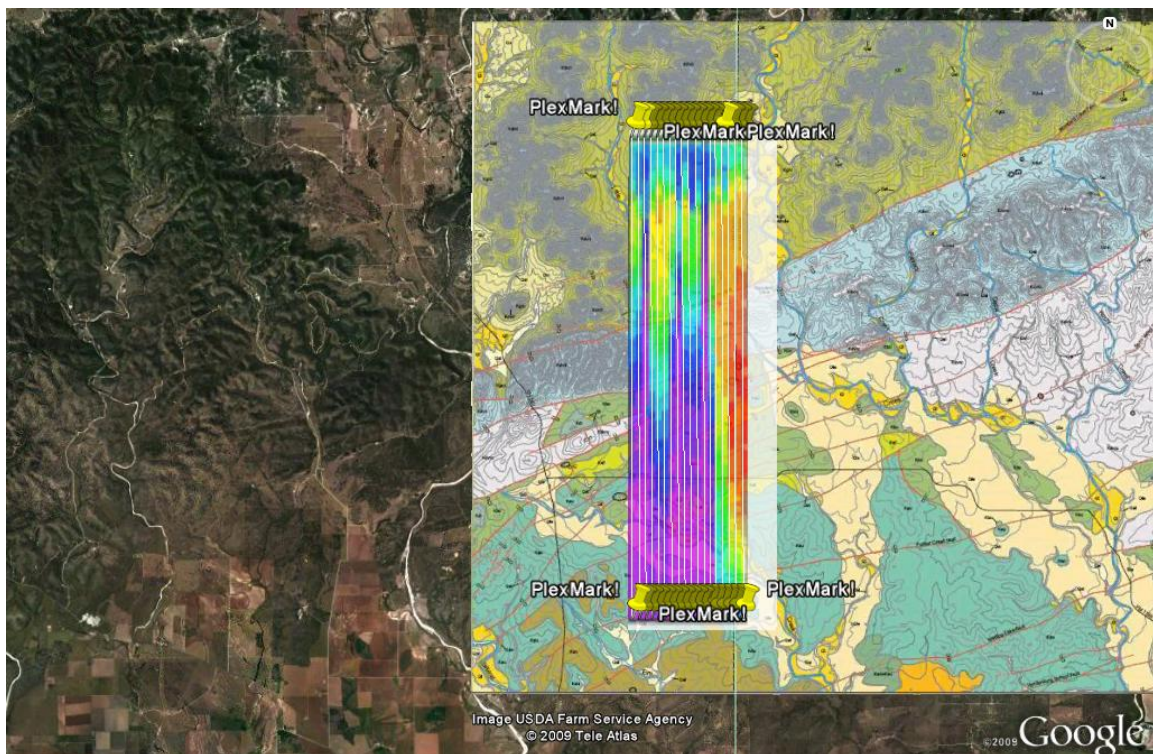


Figure A-2, continued

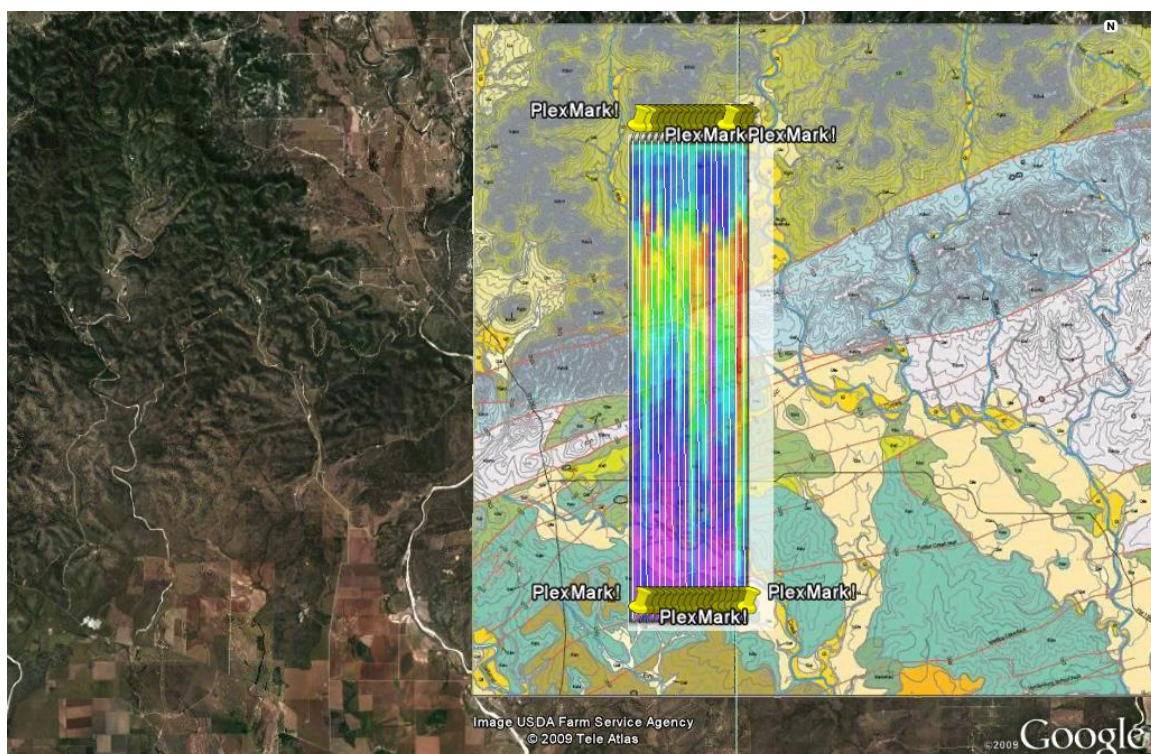


25 kHz

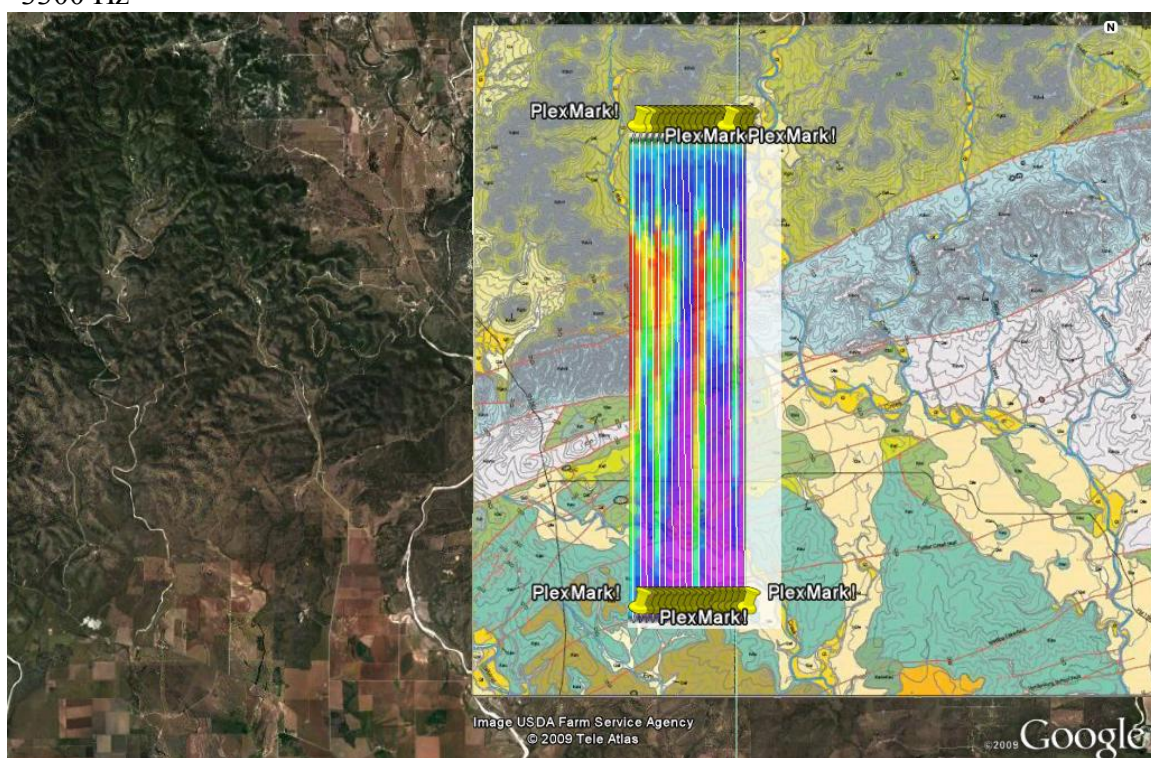


6200 Hz

Figure A-3: Additional maps of β_H as overlays on geological map of survey area.



3300 Hz



1500 Hz

A-3, continued

VITA

Name: Kathryn Teresa Decker

Address: 4 Forest Road
Utica, NY 13501

E-mail Address: *kdecker27@gmail.com*

Education: B.S., Geology – Geophysics, Binghamton University, 2003
B.A., Mathematics – Binghamton University, 2003
M.S., Geophysics – Texas A&M University, 2009